Department of Advanced Materials Science,
Graduate School of Frontier Sciences,
The University of Tokyo

Master's Thesis

Generation of Large Spin Accumulation and Its Application to Superconductivity Modulation

巨大スピン蓄積の生成と超伝導状態制御

January 24, 2012
Supervisor: Prof. YoshiChika Otani

47-106045　Taro Wakamura

Contents

Chapter 1

Introduction

1.1 Historical review of spintronics

In the first section of this chapter, we briefly date back to the birth of the spintronics. Although the name of *spintronics* does not have a long history, its concept itself naturally derives from the condensed matter physics.

1.1.1 Discovery of GMR effect

Condensed matter physics has now become quite essential in terms both of a fundamental science and of its applications to practical devices. As the fundamental science, condensed matter physics aims to investigate physical phenomena occurred in a wide variety of materials, from metals, semiconductors and magnetic materials and down to exotic materials intensively investigated recently such as oxides, graphene and topological insulators. Among these materials, especially metals, semiconductors and magnetic materials have intimately been contributing to provide sophisticated electronic devices to our daily lives. For example, semiconductors are indispensable for recent electronic devices such as transistors, and magnetic materials are essential for memory devices now widely used in computers.

Among such significant roles of condensed matter physics, spin electronics or, spintronics is becoming one of the extending research area [1]. Spintronics is a research area which deals with physical phenomena relevant to magnetic materials and electronics. It has now become one of the promising candidates for creating novel memory devices and energy conservation devices in next generation.

The very origin of spintronics dates back to the suggestion by Mott about spin-polarized transport [2, 3]: he noticed that in magnetic materials at low temperatures sufficient to have no magnons, electron's transport could be spin-dependent because magnon scattering was neglectable. Here he also assumed that the system was clean and without magnetic impurities. In such a spin-dependent electron's transport, the

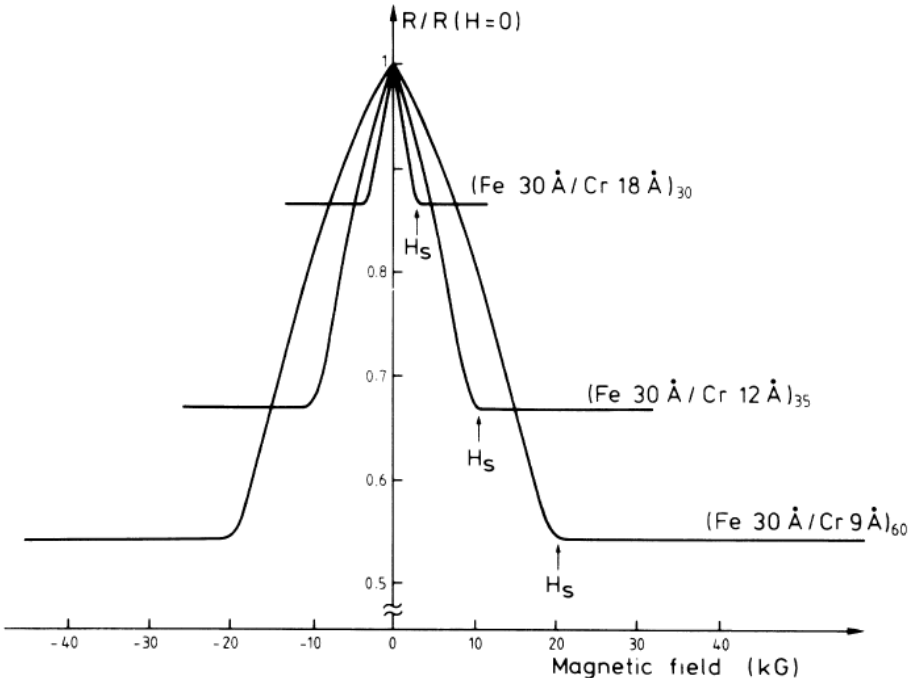

Figure 1.1: Results of GMR experiment by Baibach *et al.* [10]. In this experiment a current flows in a Cr plane. As the thickness of the Cr layer decreases, the magnetoresistance value becomes larger. This indicates the enhancement of the magnetization effect from two ferromagnets which sandwich the Cr layer.

conductivity could be expressed with the sum of two different conductivities in analogy to the two current model. These two conductivities depend on the two different direction of the spin projection to the quantization axis.

In order to investigate the spin-dependent transport in ferromagnets, a number of experiments have performed since then. In early experiments, N/F/N junctions were widely used and this trend lasted relatively long. Here N denotes nonmagnetic metal and F denotes ferromagnet. Moodera *et al.*, for example, found that a current passing through the ferromagnetic semiconductor can become spin-polarized [4]. Superconductor(S) has been also used for measuring the spin polarization of F. Tedrow *et al.*, used Zeeman-split quasiparticle states in S for detecting the spin polarization of various magnetic materials [5, 6, 7].

In the next stage, F/N/F or F/I/F tunnel junction has become a field for measuring spin-dependent transport. I denotes insulator. Julliere measured a tunneling conductance of F/I/F tunnel junctions and made a model for describing the resistance difference between the parallel/antiparallel magnetization state of two Fs [8]. Although this model was found inadequate to explain some experimental results accurately, it absolutely attracted the attention to the spin-dependent transport [9].

A big breakthrough has emerged with the experiment performed by Baibach *et*

al. [10]. They found that in flowing an in-plane current through the N part of the F/N/F multi layer structure, the resistance changed according to the parallel/antiparallel magnetization configuration between the two F layers. Although in the early stages of experiment they flowed a current in-plane, later a current flowing perpendicularly to the layer structure has then technically achieved. It was then found out that the current-out-of-plane geometry provides more difference in the resistance [11]. This large resistance difference relevant to the magnetization orientation of two F layers is named *giant magneto-resistance*(GMR). The first discovery of the GMR effect activates a great number of both theoretical and experimental studies. The GMR ratio, the difference in resistance between two different magnetization alignments, increased as the research progressed [12, 13]. After the observation of the room temperature GMR effect a lot of new researches started aiming to the application of GMR effect to memory devices [14, 15].

Subsequently using an insulator in stead of a nonmagnetic metal was found to improve the GMR ratio. The GMR effect observed in the F/I/F structure is called *tunnel magneto-resistance*(TMR) effect named after the contribution from tunneling electrons through I. Especially, it was theoretically predicted that using MgO as a tunneling layer generates a high TMR ratio [16]. It was experimentally confirmed and the TMR ratio reached up to 250 % by the two groups independently [17, 18]. This increasing value opens a way to memory devices such as a magnetic random access memory (MRAM) with a higher performance. The discovery of GMR effect is generally regarded as a birth of modern spintronics.

1.1.2 Spin injection experiments

In a stream of the intensive research about the large magnetoresistance effect, the first experiment about an injection into a spin-polarized current into N was performed by Johnson and Silsbee in 1985 [19]. They used an aluminum wire and deposited tiny permalloy($Ni_{81}Fe_{19}$) pads on it. The center-to-center distance between the pads was in multiples of 50 μm. The two pads were used as a spin injector and a spin detector. They pointed out that in flowing a current from one of the pads ($x = 0$) to another pad ($x = -L$) through the aluminum wire, the current is spin-polarized, and the nonequilibrium spins also defuse to the area $x > 0$. In $x > 0$, there are no flows of a charge current in the sample configuration. By sweeping the external magnetic field parallel to the magnetization axis of the pads, a finite voltage difference was detected between the parallel/antiparallel magnetization configuration of the detector and the injector (see Fig. 1.3). From the distance dependence of the detected voltage they obtained the spin diffusion length of hundreds nanometers. They also performed the

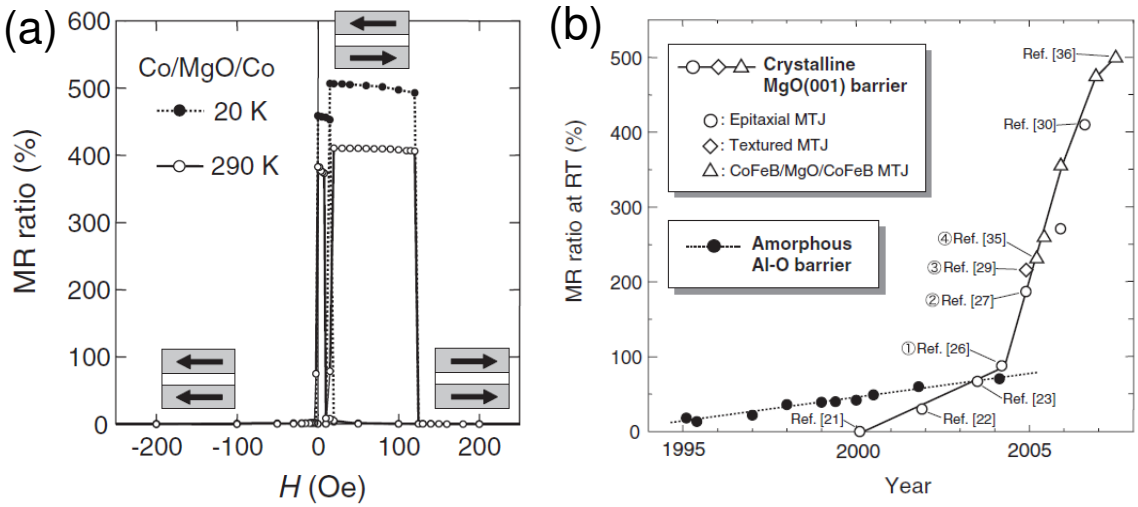

Figure 1.2: (a): Hundred percent order magnetoresistance obtained at 20 K and 290 K in epitaxial Co/MgO/Co structures, accompanied by the magnetization configuration of two Co layers. (b): Progress of the GMR experiment from 1995 to 2008. The highest value more than 500 % was obtained.

Hanle experiment applying an external magnetic magnetic field at an angle of ϕ toward the vertical axis of the sample plane. The results showed a clear sinusoidal dependence of the detected voltage on the angle ϕ, which indicated that the out-of-plane part of the magnetic field contributes to the rotation of the electrons' spin. We note that in this experiment the value of the voltage was quite small (an order of picovolts).

After the early stages of experiments, the spin injection was performed into other kinds of material, such as semiconductor or superconductor [20, 21, 22, 23, 24, 25, 26]. As for the metallic systems, thin-film geometry became popular and ingenious sample structures such as "bipolar spin switch" were suggested [27].

1.1.3 Electrical spin injection and detection at room temperature in nanoscale samples

Although Johnson and Silsbee successfully demonstrated the experiments of the electrical spin injection and the detection, they were performed only at low temperature ($\sim$77 K) and the spin accumulation signal was too small to detect easily. After this experiment, most of the spin injection/detection experiments were performed by using an optical technique [28, 29, 30] and no electrical spin injections/detections have been done for about two decades in metallic systems.

In 2001, Jedema *et al.* first showed the electrical spin injection and the detection at room temperature by using nanoscale lateral spin valves (see. Fig. 1.4) [39]. They measured the spin accumulation signal nonlocally and obtained typical NLSV signals

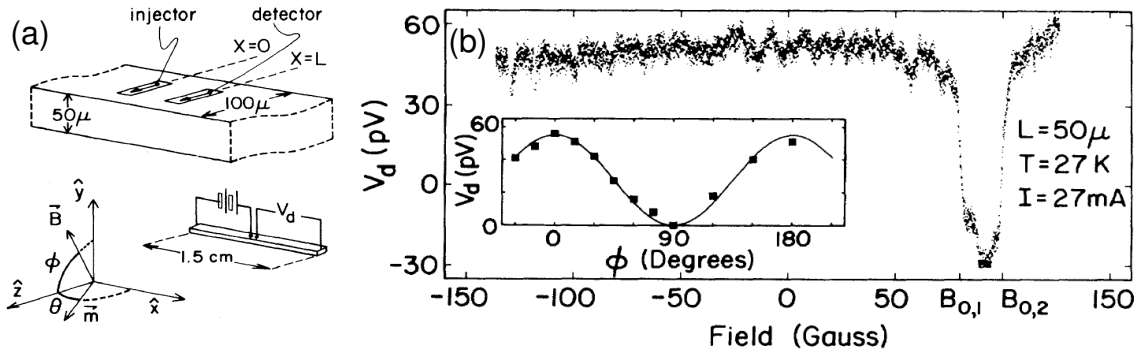

Figure 1.3: The first spin injection experiment by Johnson and Silsbee is shown [19]. (a): Sample structure. Two Py islands are on a bulk Al. A current flows between Py and Al, and a voltage is nonlocally detected between Py and Al at the other side. (b): Detected voltage. An antiparallel magnetization state generates a voltage difference $\sim$ 75 pV at $T = 27$ K. (Inset): Results of the Hanle effect measurements. Vertical axis denotes the angle of the external magnetic field.

($\sim$ 0.4 mΩ at 293 K). They also demonstrated the electrical Hanle measurements in Co/Al/Co nanoscale spin valve samples and showed the consistency of the physical parameters with those obtained from the NLSV measurements [40]. These two attractive demonstrations brought the intensive studies of the electrical spin injection and the detection both at low temperature and at room temperature in this decade.

1.2 Theoretical background of spintronics

1.2.1 Spin-polarized transport

In order to understand the spin transport in materials, we start with the notion of the spin polarization and the spin-polarized transport. Due to the magnetization, in F, electrons with different spin directions have a different density of states at the Fermi energy (see Fig. 1.5(a)). This difference results in a spin-polarized current in F.

Provided that a current flows between F and N, the spin-polarized current induces a spin accumulation, namely, the chemical potential difference of up-spin and down-spin electrons. In the F side, this chemical potential difference is soon equilibrated through the strong exchange interaction. However, in N the difference persists within a relatively longer (sometimes an order of a micrometer) distance from the interface of the F and N junction (Fig. 1.5(b)) . This spin accumulation is one of the key quantities in spintronics as discussed below.

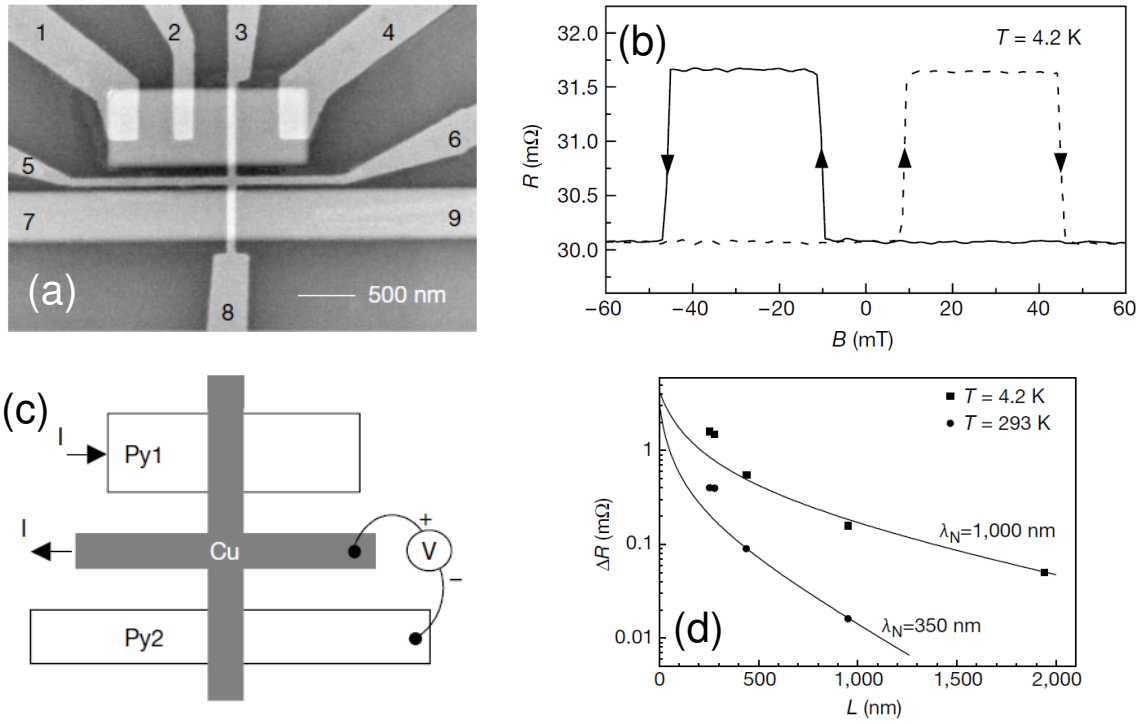

Figure 1.4: Configurations and results of nonlocal spin signal measurements are shown [37]. (a): SEM image of the sample. In the NLSV measurements a current flowed between contact 1 and 5, and a voltage between contacts 6 and 9 was detected. (b): Typical NLSV signal at 4.2 K. (c): Schematic illustration of the sample. Two Py strips have different shape to have different coercive fields. (d) distance dependence of the NLSV signals. Spin diffusion length λ_N was determined as 1000 nm at 4.2 K and 350 nm at 293 K.

1.2.2 Spin relaxation mechanism

Spin relaxation and spin dephasing are one of the important issues in spintronics. Via these processes electron's spins are equilibrated in metals and semiconductors. There are mainly four mechanisms which contribute to spin relaxation: the Elliott-Yafet mechanism, the D'yakonov-Perel' mechanism, the Bir-Aronov-Pikus mechanism and the hyperfine interaction [31]. Since the Elliott-Yafet mechanism is the most relevant to the metallic systems, we mainly introduce the Elliott-Yafet system and briefly discuss the other mechanisms.

In the Elliott-Yafet process electron's spin of one direction couples with another spin state via the spin-orbit(SO) coupling with lattice ions. Elliott pointed in 1954 if there is a SO coupling between lattice ions and conduction electrons, electrons' spin can relax via ordinary momentum scattering such as phonon or impurity scattering [32].

The SO coupling has a general form as follows:

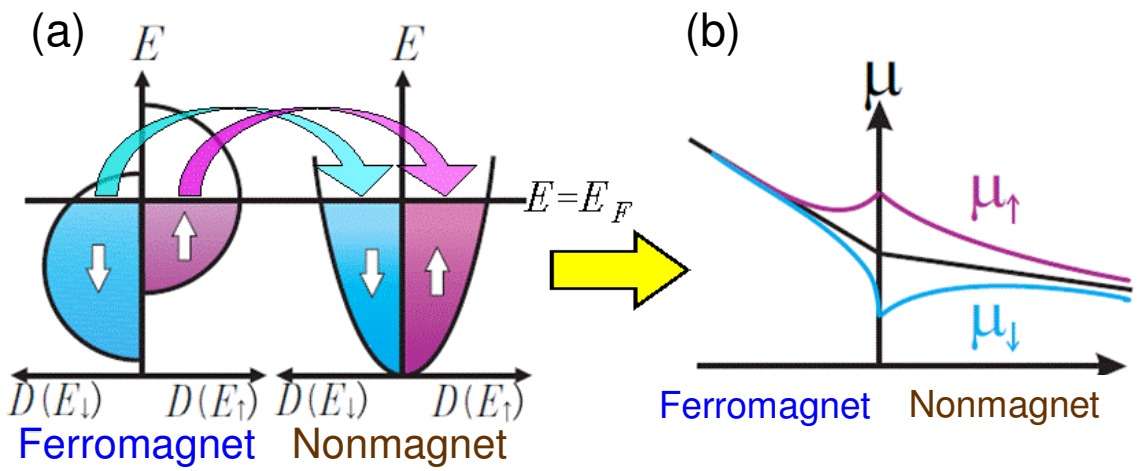

Figure 1.5: (a): Schematic illustration of the density of the states of a ferromagnet and a nonmagnet (both simplified). The difference of the density of the states at the Fermi level causes the spin-polarized transport. (b): Spin accumulation is described as a difference in chemical potential. This difference is sustained in a longer distance in the nonmagnet.

$$V_{SO} = \frac{\hbar}{4m^2c^2}(\nabla V_{SC} \times \mathbf{p}) \otimes \sigma, \tag{1.1}$$

where m is the free-electron mass, V_{SC} is the scalar (spin-independent) periodic lattice potential, $\mathbf{p} \equiv -i\hbar\nabla$ is the linear momentum operator, and σ are the Pauli matrices, respectively.

Due to the SO coupling, the electron's spin and its momenta correlate, and the spin-up state $|\uparrow\rangle$ and the spin-down state $|\downarrow\rangle$ are no longer the eigenstates of σ_z. Therefore, the Bloch wave functions in solids are modified as follows:

$$\Psi'_{\mathbf{k}\uparrow}(\mathbf{r}) = \alpha_{\mathbf{k}}(\mathbf{r})|\uparrow\rangle + \beta_{\mathbf{k}}(\mathbf{r})|\downarrow\rangle \tag{1.2}$$

$$\Psi'_{\mathbf{k}\downarrow}(\mathbf{r}) = \xi_{\mathbf{k}}(\mathbf{r})|\uparrow\rangle + \eta_{\mathbf{k}}(\mathbf{r})|\downarrow\rangle, \tag{1.3}$$

where $\Psi'_{\mathbf{k}\uparrow}(\mathbf{r})$ and $\Psi'_{\mathbf{k}\downarrow}(\mathbf{r})$ are the states which originally have $|\uparrow\rangle$ and $|\downarrow\rangle$ in the spin states, respectively. Mixing with another spin state is therefore determined by the ratio between the coefficients of the original spin state and another spin state. For example, for the Bloch wave function $\Psi'_{\mathbf{k}\uparrow}(\mathbf{r})$, the value of $\beta_{\mathbf{k}}(\mathbf{r})$ determines the strength of the mixing. A perturbative calculation leads to the results of $\beta_{\mathbf{k}}(\mathbf{r}) \sim \lambda_{SO}/\Delta E \ll 1$, where ΔE denotes the difference between two energy bands of the same $\mathbf{k}$ and λ_{SO} the matrix element of V_{SO} between them. This result reflects the fact that the energy scale of V_{SO}

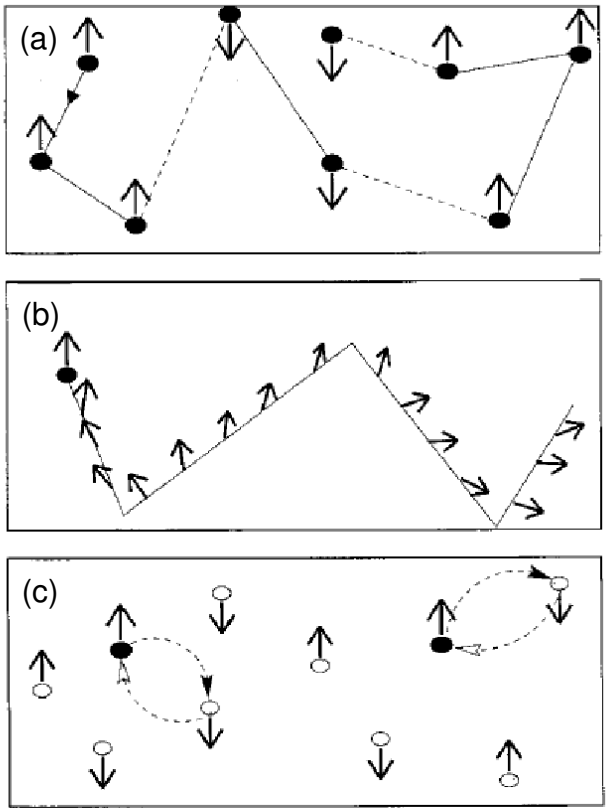

Figure 1.6: Three spin-relaxation mechanisms are shown [31]. (a): Elliott-Yafet mechanism. along the electron's travel, its spin flips at the moment of momentum scattering. (b): D'yakonov-Perel' mechanism. An electron strolls, always feeling an effective magnetic field. Its spin thus continuously dephases according to the gradual change of its momenta. (c): Bir-Aronov-Pikus mechanism. Black dots represent electrons and white dots holes. The exchange coupling between an electron and a hole causes the spin relaxation.

is generally much less than the energy difference between the two neighboring energy bands. Thus ordinarily we can neglect the mixing and regard $\Psi'_{\mathbf{k}\uparrow}(\mathbf{r})$ as the spin-up state.

However, in certain conditions, the value of $\beta_{\mathbf{k}}(\mathbf{r})$ becomes effective. Although the SO coupling itself does not cause spin relaxation, the combination with momentum scattering makes it effective. Momentum scattering is usually caused by a scattering with phonons or impurities. In combination with the phonon-mediated spin-relaxation mechanism suggested by Yafet, a consistent picture of the phonon-induced spin relaxation has established [33].

The spin relaxation of the Elliott-Yafet mechanism is characterized by the spin relaxation time τ_s. There are two important relation which gives an order of magnitude of τ_s. One is the "Elliott relation" and gives the relative relation between τ_s and τ_p. Here τ_p represents the momentum relaxation time. After the Born approximation, one

obtains

$$\frac{1}{\tau_s} \sim \frac{\beta^2}{\tau_p}. \tag{1.4}$$

Here we emphasize that τ_s linearly depends on τ_p. Another important relation is called "Yafet relation", and expresses as

$$\frac{1}{\tau_s} \sim \beta^2 \rho(T). \tag{1.5}$$

This equation shows that the temperature dependence of τ_s is an inverse of that of the resistivity. We note that the momentum scattering is dominated by the phonon scattering at high T and by the impurity scattering at low T. This relation was experimentally confirmed by Monod and Beuneu [34].

One of the other mechanisms of the spin relaxation is the D'yakonov-Perel' mechanism. It originates from the SO coupling induced by the broken inversion symmetry of materials [35]. When the inversion symmetry is broken, the two Bloch states with the same momentum, such as $\Psi'_{\mathbf{k}\uparrow}(\mathbf{r})$ and $\Psi'_{\mathbf{k}\downarrow}(\mathbf{r})$ no longer degenerate, namely, $E_{\mathbf{k}\uparrow} \neq E_{\mathbf{k}\downarrow}$. In this regime, the energy splitting between up-spin electron and down-spin electron can be described by an intrinsic $\mathbf{k}$-dependent magnetic field $\mathbf{B}(\mathbf{k})$. This field is generally called "Dresselhaus field" and derives from the SO coupling in the band structure. Since electrons precess around this effective field, the corresponding Hamiltonian can be expressed as

$$\mathcal{H} = \frac{1}{2}\hbar\sigma \otimes \mathbf{\Omega}(\mathbf{k}), \tag{1.6}$$

where $\mathbf{\Omega}(\mathbf{k}) = (e/m)\mathbf{B}(\mathbf{k})$. Since the effective field depends on the electron's momenta$\mathbf{k}$, the electrons experiencing different momentum scattering process feel the different directions of $\mathbf{\Omega}(\mathbf{k})$. Thus this causes the spin dephasing.

The most important difference between the Elliott-Yafet mechanism and the D'yakonov-Perel' one is how τ_s depends on τ_p: in the Elliott-Yafet mechanism, $\tau_s \propto \tau_p$ as explained above, and in the D'yakonov-Perel' one, on the other hand, $\tau_s \propto 1/\tau_p$. This difference is widely used for determining the mechanism of the spin relaxation in various materials.

The other mechanisms become significant especially in semiconductors. For example, the Bir-Aronov-Pikus mechanism is relevant to the exchange interaction between electrons and holes in p-doped semiconductors [36]. The hyperfine interaction between magnetic moments of electron and nuclei is important for the spin dephasing of localized electrons such as those in quantum dots or bound on donors [37]. It is usually

trivial for itinerant electrons and is neglectable [38].

1.2.3 Nonlocal spin valve experiment

As discussed previously, the nonlocal spin valve (NLSV) experiments for the electrical spin injection and the detection is now popular since the demonstration by Jedema *et al.* [39, 40]. In this section, we theoretically describe the mechanism of the spin injection and detection in the NLSV structure.

The typical NLSV structure is shown in Fig. 1.7. Two F wires are bridged by a N strip. One of the F wires (F1) acts as a spin injector, and another F wire (F2) a spin detector. The magnetization of the wires is in single domain due to its shape anisotropy and is assumed either parallel or antiparallel. We denote the width of F and N as w_{F} and w_{N}, and thickness of F and N d_{F} and d_{N}, respectively. The two F wires are separated by the center-to-center distance of L.

Now we explain how to describe the electron transport in the NLSV structure. This description is based on [41]. Since we have two F strips, a current consists of two different parts with different spin directions. In this regime, a spin-dependent current consists of a drift part and a diffusive part: $\mathbf{j}_\sigma = \sigma_\sigma \mathbf{E} - eD_\sigma \nabla n_\sigma$, where σ_σ is the electrical conductivity of electrons with a spin σ. Here σ is either $\uparrow$ or $\downarrow$ toward z axis. e is the electron charge $e = -|e|$, n_σ is the carrier density of electrons, and D_σ is the diffusion coefficient of electrons. Using the relation $\nabla n_\sigma = N_\sigma \nabla \epsilon_F^\sigma$ and the Einstein's relation $\sigma_\sigma = e^2 N_\sigma D_\sigma$ (N_σ: the density of states in the subband, ϵ_F^σ: Fermi energy of spin σ), the current $\mathbf{j}$ can be expressed as

$$\mathbf{j}_\uparrow = -\frac{\sigma_\uparrow}{e} \nabla \mu_\uparrow \tag{1.7}$$

$$\mathbf{j}_\downarrow = -\frac{\sigma_\downarrow}{e} \nabla \mu_\downarrow, \tag{1.8}$$

where $\mu_\sigma = \epsilon_F^\sigma + e\phi$ is the electrochemical potential(ECP) and ϕ is the electric potential.

Since there is no divergence of a charge current, the continuity equation for charge and spin current in the steady(time-independent) state becomes

$$\nabla \cdot (\mathbf{j}_\uparrow + \mathbf{j}_\downarrow) = 0 \tag{1.9}$$

$$\nabla \cdot (\mathbf{j}_\uparrow - \mathbf{j}_\downarrow) = -e\frac{n_\uparrow - \bar{n}_\uparrow}{\tau_{\uparrow\downarrow}} + e\frac{n_\downarrow - \bar{n}_\downarrow}{\tau_{\downarrow\uparrow}}, \tag{1.10}$$

where $\bar{n}_\sigma$ represents the equilibrium carrier density of spin σ and $\tau_{\sigma\sigma'}$ the scattering

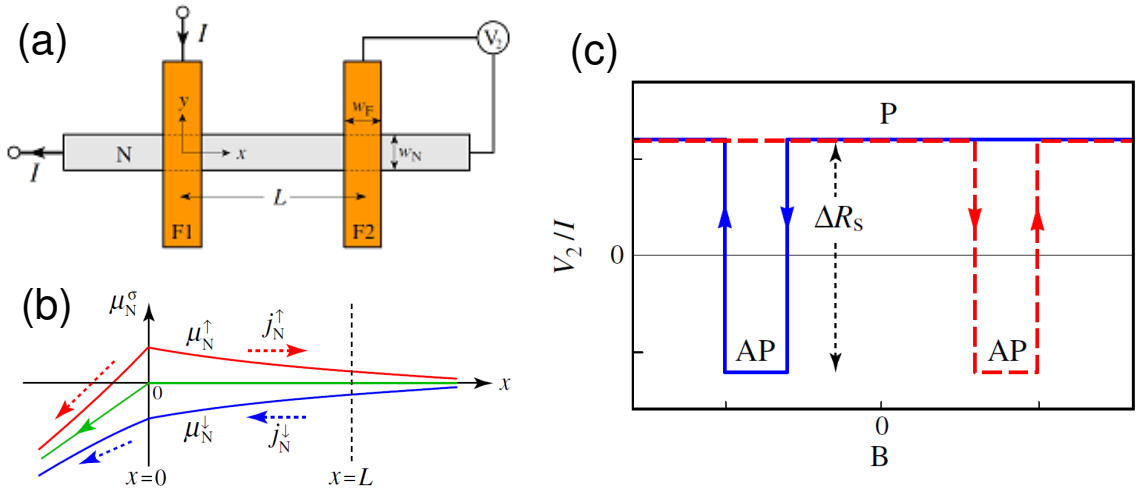

Figure 1.7: (a): Schematic illustration of the NLSV structure. A current flows between ferromagnet and nonmagnet. A voltage is detected between ferromagnet and nonmagnet at another side nonlocally. (b): chemical potential distribution of the NLSV structure. A pure spin current diffuses in the part of nonmagnet strip, where there are no charge currents. (c): Illustration of a typical NLSV signal. spin accumulation is defined by the difference in V_2/I between parallel/antiparallel magnetization of two ferromagnet strips. [42]

time of an electron from a spin state σ to σ'. Substituting these equations with the *detailed balance equation* $N_\uparrow/\tau_{\uparrow\downarrow} = N_\downarrow/\tau_{\downarrow\uparrow}$, the equations of the ECP are

$$\nabla^2(\sigma_\uparrow\mu_\uparrow + \sigma_\downarrow\mu_\downarrow) = 0 \tag{1.11}$$

$$\nabla^2(\mu_\uparrow - \mu_\downarrow) = \frac{1}{\lambda^2}(\mu_\uparrow - \mu_\downarrow). \tag{1.12}$$

Here $\lambda = \sqrt{D\tau_{sf}}$ represents the spin diffusion length with the spin-flip time and the diffusion coefficient in this regime

$$\frac{1}{\tau_{sf}} = \frac{1}{2}\left(\frac{1}{\tau_{\uparrow\downarrow}} + \frac{1}{\tau_{\downarrow\uparrow}}\right) \tag{1.13}$$

$$\frac{1}{D} = \frac{N_\uparrow/D_\downarrow + N_\downarrow/D_\uparrow}{N_\uparrow + N_\downarrow} \tag{1.14}$$

At the interface between F and N, the ECP changes discontinuously if the interface is not transparent. In order to express this ECP drop, we introduce the spin dependent interface currents

$$I_1^\sigma = \frac{1}{eR_1^\sigma}(\mu_{\rm F1}^\sigma - \mu_{\rm N}^\sigma) \tag{1.15}$$

$$I_2^\sigma = \frac{1}{eR_2^\sigma}(\mu_{\rm F2}^\sigma - \mu_{\rm N}^\sigma). \tag{1.16}$$

where R_1^σ and R_2^σ are the resistance of the interface 1 and 2, $\mu_{\rm F1}^\sigma$, $\mu_{\rm F2}^\sigma$ and $\mu_{\rm N}^\sigma$ are the chemical potential of a spin σ in F1, F2 and N, respectively. Here we assume that the current flows uniformly through the interface.

Using the equations introduced above, we can solve the distribution of the spin current $I_s = I_\uparrow - I_\downarrow$, ensured by the fact that both the charge and the spin currents conserve at each interface. As an example, when a bias current I flows from F1 to the left side of N ($I_1 = I$) and there are no charge currents on the right side of N ($I_2 = 0$), we have the solution of the ECP. In N, the ECP has a general form

$$\mu_{\rm N}^\sigma = \bar{\mu}_{\rm N} + \sigma(a_1 e^{-|x|/\lambda_{\rm N}} - a_2 e^{-|x-L|/\lambda_{\rm N}}). \tag{1.17}$$

Here $\bar{\mu}_{\rm N} = -[eI/(\sigma_{\rm N} A_{\rm N})]x$ ($A_{\rm N} = w_{\rm N} d_{\rm N}$) represents the charge transport, and therefore at $x > 0$, $\bar{\mu}_{\rm N} = 0$. The second term generates the difference between the ECP of the up-spin electrons and the down-spin electrons. In this regime, in the part of $x > 0$ in N, a spin current without charge current (named *pure spin current*) flows. In F, the ECP distributes as

$$\mu_{\rm F1}^\sigma = \bar{\mu}_{\rm F1} + \sigma b_1^\sigma e^{-z/\lambda_{\rm F}}, \tag{1.18}$$

$$\mu_{\rm F2}^\sigma = \bar{\mu_{\rm F2}} - \sigma b_2^\sigma e^{-z/\lambda_{\rm F}}. \tag{1.19}$$

In (1.19), we assume that $d_{\rm F} \gg \lambda_{\rm F}$ and $\bar{\mu}_{\rm F1} = -[eI/(\sigma_{\rm F} A_{\rm J})]z + eV_1$, $\bar{\mu}_{\rm F2} = eV_2$.

Using the condition that the charge currents ($I = I_\uparrow + I_\downarrow$) and the spin currents are continuous at the interfaces as mentioned above, we can determine the unknown coefficients. The spin-dependent voltage V_2 detected at F2 is then given by

$$V_2/I = \pm 2R_{\rm N} e^{-L/\lambda_{\rm N}} \prod_{i=1}^{2} \left(\frac{P_{\rm J}\frac{R_{\rm i}}{R_{\rm N}}}{1-P_{\rm J}^2} + \frac{p_{\rm F}\frac{R_{\rm F}}{R_{\rm N}}}{1-p_{\rm F}^2} \right) \times \left[\prod_{i=1}^{2} \left(1 + \frac{2\frac{R_{\rm i}}{R_{\rm N}}}{1-P_{\rm J}^2} + \frac{2\frac{R_{\rm F}}{R_{\rm N}}}{1-p_{\rm F}^2} \right) - e^{-2L/\lambda_{\rm N}} \right]^{-1}, \tag{1.20}$$

where $R_N = \rho_N \lambda_N / A_N$ and $R_F = \rho_F \lambda_F / A_J$ are the resistance of N and F with the cross sections A_N and A_J. λ_N and λ_F are the spin diffusion length in N and F, ρ_N and ρ_F are the resistivity of N and F, respectively. p_F is the current polarization in F. P_J denotes the polarization at the interface and is defined as $P_J = |G_i^{\uparrow} - G_i^{\downarrow}|/G_i$ with the interface conductance G_i at the interface i. + and − signs in the equation correspond to the parallel (P) and antiparallel (AP) magnetization configuration in F1 and F2. The detected spin accumulation voltage is

$$\Delta R = I^{-1}(V_2^P - V_2^{AP}) = 2|V_2|, \tag{1.21}$$

by subtracting the detected voltage divided by I in the parallel and antiparallel magnetization configuration.

1.2.4 Problems of efficient spin injection

In the NLSV experiment explained above, it is essential to inject and to detect the spin current efficiently. In 2000, Schmidt *et al.* and Rashba independently pointed out that the conductivity mismatch between F and N limits the efficient spin injection in the case of semiconductor for N (see Fig. 1.8(a)) [43, 44]. In usual cases of paramagnetic metals or semiconductors used for N, the resistance $r_N \ll r_F$, where r_N and r_F represent the resistance of normal metal and ferromagnet, respectively. In the case of the spin-dependent electronic transport, the spin resistances in N and F defined as

$$R_N = \frac{\rho_N \lambda_N}{A_N}, \quad R_F = \frac{\rho_F \lambda_F}{A_J} \tag{1.22}$$

become crucial, where ρ_X is the resistivity of X, λ_X the spin diffusion length of X. A_N is the transverse area of the strip N, and A_J is the junction area between F and N. Substituting the typical values at 10 K obtained from our group, $\rho_N \sim 2$ $\mu\Omega$cm, $\rho_F \sim 20$ $\mu\Omega$cm, $\lambda_N = 1.3$ μm, $\lambda_F = 5$ nm, A_N and $A_J = 2.0 \times 10^{-14}$ m^2, the ratio $\frac{R_N}{R_F} \sim 30$. Therefore, compensating "the spin resistance mismatch" between N and F is essential to enhance the efficiency of the spin injection or detection in N. Several theoretical studies showed that the insertion of an insulating layer between N and F compensated the mismatch and assisted to enhance the spin accumulation signal. In order to discuss this problem, we refer to (1.20). When one of the F/N junctions is tunneling like and another is transparent ($R_1 \ll R_F \ll R_N \ll R_2$ or $R_2 \ll R_F \ll R_N \ll R_1$), the spin accumulation becomes

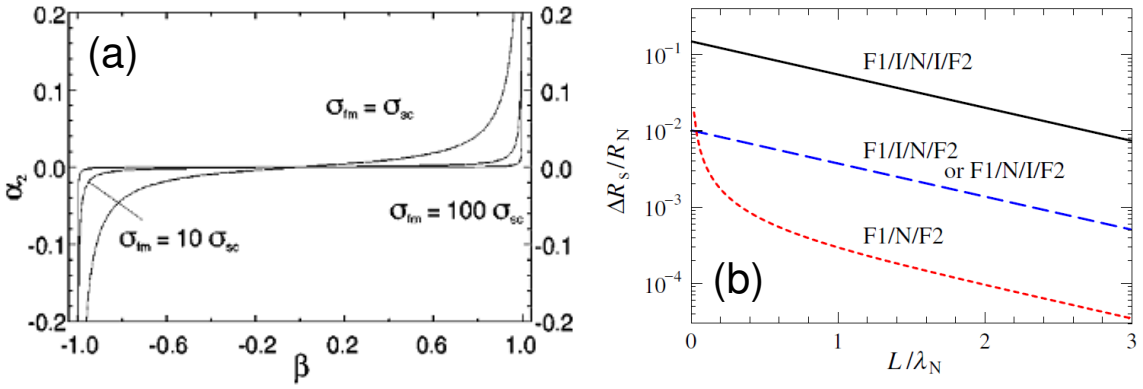

Figure 1.8: Dependence of the spin accumulation signal on the interface between F and N. (a): Results of calculation in F/N(semiconductor)/F structure first proposed by Schmidt *et al.* [43]. α_2 and β represents the spin polarization of the semiconductor and the ferromagnet. (b): Theoretical results of metallic system. Insertion of an insulating layer (I) between F and N clearly enhances the spin accumulation [42].

$$\Delta R = \frac{2p_{\mathrm{F}}P_{\mathrm{J}}}{(1-p_{\mathrm{F}}^2)} R_{\mathrm{N}} \left(\frac{R_{\mathrm{F}}}{R_{\mathrm{N}}}\right) e^{-L/\lambda_{\mathrm{N}}}. \tag{1.23}$$

If we assume the interface at both junctions between F and N as tunneling like ($R_1, R_2 \gg R_{\mathrm{N}}$), we obtain

$$\Delta R = P_{\mathrm{J}}^2 R_{\mathrm{N}} e^{-L/\lambda_{\mathrm{N}}}. \tag{1.24}$$

We note that by assuming the tunnel junction between F and N, we can omit the term $R_{\mathrm{N}}/R_{\mathrm{F}}$. The distance dependence of the spin accumulation in N with different junction conditions is shown in (Fig. 1.8(b)). Theoretical calculations explicitly show the enhancement of the spin accumulation by the tunneling F/N junctions. Several experimental studies followed these results. Recently, Fukuma *et al.* have demonstrated the enhancement of the spin accumulation signal by about ten times through the insertion of the MgO layer in Py/Ag/Py NLSV systems [45]. They subsequently showed that annealing the sample helps the MgO layer well-textured and the amount of the enhancement beccomes anomalously large [46]. These studies open a new way to attain future spintronic devices.

1.3 Fundamentals of superconductor

Superconductivity is now one of the important physical phenomena and universal to various kinds of materials. Since Kamerlingh Onnes first found the electrical resistance of a mercury dropped to zero at 4.2 K [47], superconductivity has been attracting many

researchers [48]. Through the early experiments, they found that superconductivity was not phenomenon typical to certain materials, but very common to many types of material. Research of superconductivity went into the new stage especially after Bednorz and Müller had found a "high-T_c superconductor" [49]. Theoretical researches of superconductivity have also been proceeding, but many exotic phenomena especially relevant to the high-T_c superconductors have not yet been understood. In this section, we briefly introduce the fundamental properties and the theories of superconductivity, especially superconductivity of metals.

1.3.1 GL theory and BCS theory

The Ginzburg-Landau(GL) theory is one of the successful theories which can explain the superconductivity by using a phenomenological macroscopic order parameter and useful to analyze the superconductivity in a nonuniform situation [50]. The superconductivity state is described by the free energy of the entire system. If we define $\Psi(\mathbf{r})$ as the order parameter, we can express the free energy of the system in analogy to the thermal physics as follows

$$\mathcal{F}(\Psi) = \mathcal{F}_0 + \alpha|\Psi|^2 + \frac{\beta}{2}|\Psi|^4 + \frac{1}{2m^*}\left|\left(\frac{\hbar}{i}\nabla - \frac{e^*}{c}\mathbf{A}\right)\Psi\right|^2 + \frac{h^2}{8\pi}, \tag{1.25}$$

where α and β are coefficients, and m^*, e^* and $\mathbf{A}$ are the effective mass, the effective charge of electrons, and the vector potential, respectively. When we assume a homogeneous order parameter and no external fields, (1.9) becomes

$$\mathcal{F}(\Psi) = \mathcal{F}_0 + \alpha|\Psi|^2 + \frac{\beta}{2}|\Psi|^4 \tag{1.26}$$

Subject to $\delta\mathcal{F}/\delta\Psi = 0$, we can determine Ψ as

$$\Psi = 0 \quad (T > T_c) \tag{1.27}$$

$$\Psi = \sqrt{\frac{\alpha}{\beta}} = \sqrt{\frac{a(T_c - T)}{\beta}} \quad (T < T_c), \tag{1.28}$$

and we can plot $\mathcal{F}$ vs Ψ as in Fig. 1.9. In this equation we assume that α is temperature-dependent and can be written as $\alpha = a(T_c - T)$, considering the phase transition at the critical temperature T_c.

The other important theory for describing superconductivity is the Bardeen-Cooper-

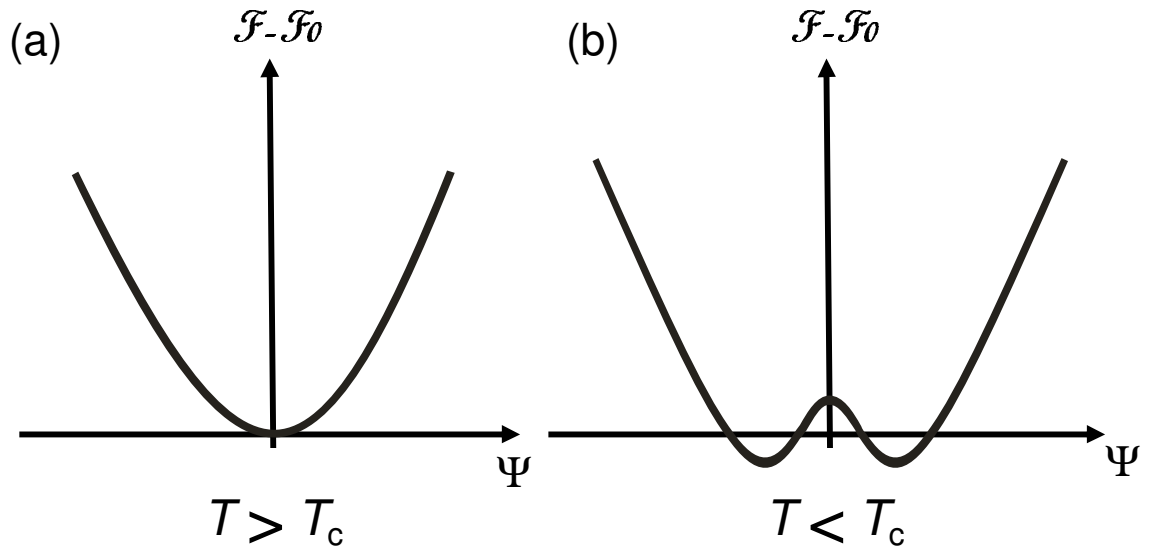

Figure 1.9: Relation between system's free energy and order parameter Ψ. (a): When $T > T_c$, there is only one energy minimum at $\Psi = 0$. (b): When $T < T_c$, there are two energy minima at finite values of Ψ.

Schrieffer(BCS) theory [51]. The basic idea is relevant to Bose-Einstein condensation of electrons' pairs, suggested by Cooper in 1956 [52]. He theoretically showed that even a weak attraction could bind pairs of electrons. This means that with some weak attraction the Fermi sea becomes unstable and the ground state becomes different from that of ordinary metals. Therefore a redistribution can occur which is energetically favorable considering the attractive potential among electrons. In the presence of electronic correlation, Hamiltonian is generally described as

$$\mathcal{H} = \sum_{\mathbf{k}\sigma} \epsilon_{\mathbf{k}} a^{\dagger}_{\mathbf{k}\sigma} a_{\mathbf{k}\sigma} + \frac{1}{2} \sum_{\mathbf{k}\mathbf{k}'\mathbf{q}\sigma\sigma'} V_{\mathbf{k}\mathbf{k}'\mathbf{q}\sigma\sigma'} a^{\dagger}_{\mathbf{k}-\mathbf{q}\sigma} a^{\dagger}_{\mathbf{k}'+\mathbf{q}\sigma'} a_{\mathbf{k}'\sigma'} a_{\mathbf{k}\sigma} \tag{1.29}$$

In the normal state, the ground state is the state in which electrons are filled in Fermi sphere. This is described as

$$|\psi_{g0}\rangle = \prod_{|\mathbf{k}|<k_F} a^{\dagger}_{\mathbf{k}\uparrow} a^{\dagger}_{\mathbf{k}\downarrow} |\phi_{n0}\rangle \tag{1.30}$$

Considering the pairing of the electrons induced from the attractive potential, Cooper assumed no kinetic energies of pairs(no momenta of each pair) as a ground state. Thus by transforming (1.30), a trial function of the BCS ground state is represented as

$$|\psi_g\rangle = \prod_{\mathbf{k}} (|u_{\mathbf{k}}| + |v_{\mathbf{k}}| e^{i\varphi} a^{\dagger}_{\mathbf{k}\uparrow} a^{\dagger}_{-\mathbf{k}\downarrow} |\phi_0\rangle. \tag{1.31}$$

In this state the number of electrons (N) is undetermined and as a result a finite phase $e^{i\varphi}$ is added following $|v_{\mathbf{k}}|$. This phase is relevant to uncertainty principle $\Delta N \Delta\varphi > 1$. For the normalization, the variable coefficients $|u_{\mathbf{k}}|$ and $|v_{\mathbf{k}}|$ fulfill $|u_{\mathbf{k}}|^2 + |v_{\mathbf{k}}|^2 = 1$. In order to determine the ground state, we transform the Hamiltonian (1.29) into the equation as follows

$$\mathcal{H} = \sum_{\mathbf{k}\sigma} \epsilon_{\mathbf{k}} a^{\dagger}_{\mathbf{k}\sigma} a_{\mathbf{k}\sigma} + \sum_{\mathbf{k}\mathbf{k}'} V_{\mathbf{k}\mathbf{k}'} a^{\dagger}_{\mathbf{k}\uparrow} a^{\dagger}_{-\mathbf{k}\downarrow} a_{-\mathbf{k}'\downarrow} a_{\mathbf{k}'\uparrow}. \tag{1.32}$$

In the equation we ignore many other terms which involve electrons not paired as ($\mathbf{k}$,$-\mathbf{k}$) in (1.32) because they do not contribute to the condensation. We substitute a transformation of $a_{-\mathbf{k}\downarrow} a_{\mathbf{k}\uparrow} = \langle a_{-\mathbf{k}\downarrow} a_{\mathbf{k}\uparrow} \rangle + a_{-\mathbf{k}\downarrow} a_{\mathbf{k}\uparrow} - \langle a_{-\mathbf{k}\downarrow} a_{\mathbf{k}\uparrow} \rangle$ into (1.32), and ignore second order term of the deviation from the average value ($a_{-\mathbf{k}\downarrow} a_{\mathbf{k}\uparrow} - \langle a_{-\mathbf{k}\downarrow} a_{\mathbf{k}\uparrow} \rangle$), then we obtain

$$\mathcal{H} = \sum_{\mathbf{k}\sigma} \epsilon_{\mathbf{k}} a^{\dagger}_{\mathbf{k}\sigma} a_{\mathbf{k}\sigma} + \sum_{\mathbf{k}\mathbf{k}'} V_{\mathbf{k}\mathbf{k}'} \{ a^{\dagger}_{\mathbf{k}\uparrow} a^{\dagger}_{-\mathbf{k}\downarrow} \langle a_{\mathbf{k}'\downarrow} a_{-\mathbf{k}'\uparrow} \rangle + \langle a^{\dagger}_{\mathbf{k}\uparrow} a^{\dagger}_{-\mathbf{k}\downarrow} \rangle a_{-\mathbf{k}\downarrow} a_{\mathbf{k}\uparrow} - \langle a^{\dagger}_{\mathbf{k}\uparrow} a^{\dagger}_{-\mathbf{k}\downarrow} \rangle \langle a_{\mathbf{k}'\downarrow} a_{-\mathbf{k}'\uparrow} \rangle \}. \tag{1.33}$$

Next we define the gap potential $\Delta_{\mathbf{k}}$ as $\Delta_{\mathbf{k}} = \sum_{\mathbf{k}'} V_{\mathbf{k}\mathbf{k}'} \langle a_{-\mathbf{k}'\downarrow} a_{\mathbf{k}'\uparrow} \rangle$. Then (1.33) becomes

$$\mathcal{H} = \sum_{\mathbf{k}\sigma} \epsilon_{\mathbf{k}} a^{\dagger}_{\mathbf{k}\sigma} a_{\mathbf{k}\sigma} - \sum_{\mathbf{k}} \{ \Delta_k a^{\dagger}_{\mathbf{k}\uparrow} a^{\dagger}_{-\mathbf{k}\downarrow} + \Delta^{*}_{\mathbf{k}} a_{-\mathbf{k}\downarrow} a_{\mathbf{k}\uparrow} - \Delta_{\mathbf{k}} a^{\dagger}_{\mathbf{k}\uparrow} a^{\dagger}_{-\mathbf{k}\downarrow} \}. \tag{1.34}$$

(1.34) can be diagonalized by using Bogoliubov transformation:

$$a_{\mathbf{k}\uparrow} = u^{*}_{\mathbf{k}} \gamma_{\mathbf{k}0} + v_{\mathbf{k}} \gamma^{\dagger}_{\mathbf{k}1} \tag{1.35}$$

$$a^{\dagger}_{-\mathbf{k}\downarrow} = -v^{\dagger}_{\mathbf{k}} \gamma_{\mathbf{k}0} + u_{\mathbf{k}} \gamma^{\dagger}_{\mathbf{k}1}. \tag{1.36}$$

$$\tag{1.37}$$

After substitution, one finally obtains

$$\mathcal{H} = \sum_{\mathbf{k}} (\epsilon_{\mathbf{k}} - E_{\mathbf{k}} + \Delta_{\mathbf{k}} \langle a_{-\mathbf{k}\downarrow} a_{\mathbf{k}\uparrow} \rangle) + \sum_{\mathbf{k}} E_{\mathbf{k}} (\gamma^{\dagger}_{\mathbf{k}0} \gamma_{\mathbf{k}0} + \gamma^{\dagger}_{\mathbf{k}1} \gamma_{\mathbf{k}1}). \tag{1.38}$$

The first term is constant, and the second term represents the excitation from the

ground state by using the Fermionic creation/annihilation operator of quasiparticles. Therefore, the BCS ground state can be regarded as a vacuum state for the quasiparticles. Here $E_{\mathbf{k}} = \sqrt{\xi_{\mathbf{k}}^2 + \Delta_{\mathbf{k}}^2}$ represents excitation spectrum of quasiparticles. Thus there is a finite gap $\Delta_{\mathbf{k}}$ for the excitation of superconductors.

1.3.2 Josephson junction

Josephson junction is one of the significant fields in which one can find the macroscopic coherence of superconductors [53, 54]. As mentioned in the previous section, the coherent state of a superconductor is characterized by the GL order parameter $\Psi = |\Psi|e^{i\varphi}$. At an equilibrium state of bulk superconductors, the phase φ of the order parameter is constant. On the other hand, provided that two superconductors sandwich a thin insulating layer or normal metal, it is possible that these superconductors weakly couple through the interchange of Cooper pairs each other. If there are no phase differences of the order parameter between the two superconductors, the situation is the same as that in bulk materials at equilibrium. However, if there IS a finite phase difference, this state should be nonequilibrium state and as a result the interchange of Cooper pairs occurs. In 1962, Josephson predicted that a zero voltage supercurrent could flow through the junction along the relation

$$I = I_c \sin \Delta\varphi, \tag{1.39}$$

where $\Delta\varphi = \varphi_1 - \varphi_2$, which denotes the phase difference between the order parameter of two superconductors. He also predicted when there is a voltage drop in the junction, the relation between the voltage and the phase difference become

$$\frac{d\Delta\varphi}{dt} = \frac{2eV}{\hbar}. \tag{1.40}$$

By using these two fundamental equations, one can describe a realistic situation of the junction. In experiments, one flows a bias current through the junction, and there is a finite voltage drop at a finite temperature due to the thermal quasiparticle excitation. The equivalent model for explaining this situation is called "RCSJ model" [55, 56] and can be represented as

$$I = I_{c0} \sin \varphi + \frac{V}{R} + C\frac{dV}{dt}, \tag{1.41}$$

where we redefine the phase difference as φ. The first term is from the supercurrent

in the junction, and the second term is due to the thermal excitation of quasiparticles. We also have the third term because the junction can be regarded as a capacitor. Using the relation of (1.40),(1.41) becomes

$$I = I_{c0} \sin\varphi + R^{-1} \frac{2e}{\hbar} \frac{d\varphi}{dt} + C \frac{2e}{\hbar} \frac{d^2\varphi}{dt^2}. \tag{1.42}$$

Introducing a dimensionless variable $\tau = \omega_p t$, where $\omega_p = (2eI_{c0}/\hbar C)$, (1.42) becomes

$$\frac{d^2\varphi}{d\tau^2} + \mathcal{Q}^{-1} \frac{d\varphi}{d\tau} + \sin\varphi = \frac{I}{I_{c0}}, \tag{1.43}$$

where

$$\mathcal{Q} = \omega_p RC. \tag{1.44}$$

In analogy to the classical kinetic equation, (1.43) can be regarded as a kinetic equation for a particle of mass $(\hbar/2e)^2 C$ moving along the φ axis at a time τ in an effective potential

$$U(\varphi) = -E_J \cos\varphi - \frac{\hbar I}{2e}\varphi, \tag{1.45}$$

where $E_J = (\hbar/2e)I_{c0}$, with a viscous drag force $(\hbar/2e)^2 R^{-1} d\varphi/dt$. The potential is called "*washboard potential*", named after its shape as shown in Fig. 1.10(a). At an equilibrium, the particle stays at the hollow of the wavy potential. A generation of a finite voltage means an escape off the hollow. Explicitly, twice value of E_J represents the hight of the barriers. Therefore the strength of the coupling between two superconductors is determined by the value of E_J. This equivalently means the stability of the particle in the hollow depends on E_J. The slope of the potential originates from the bias current I. As I increases, the junction turns into the voltage state. These descriptions are consistent with the experimental results. The change from the voltage state to the superconducting state has two different regime, according to the relative value of the capacitance C of the junction to its resistance: one is underdamped regime, in which a viscous drag force is so small that a running particle is not easy to be trapped. Another regime is overdamped regime, in which a viscous force is enough to trap the running particle. Because of this damping difference, the I-V curve of the junction become hysteric or non-hysteric, respectively. In our experimental configuration, the junction is in overdamped regime due to its smaller capacitance.

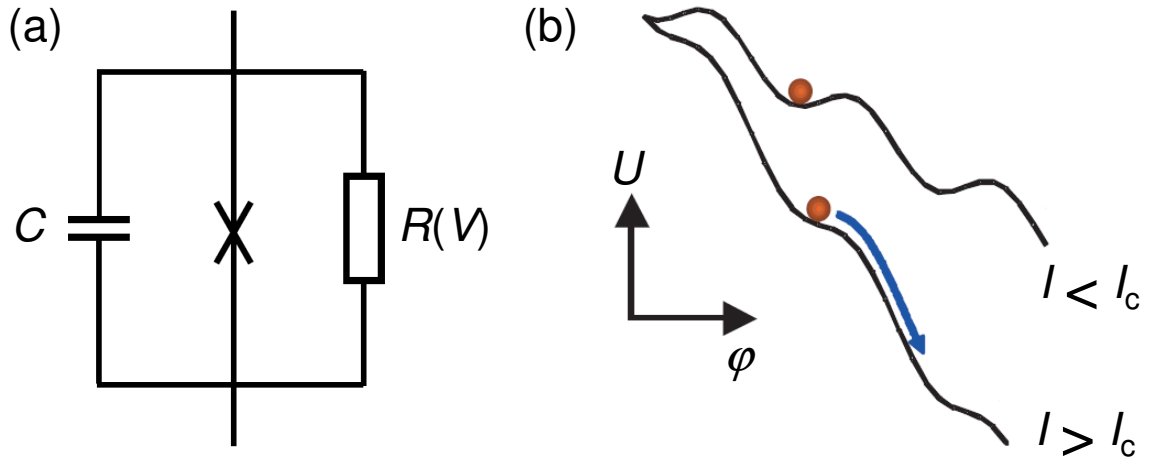

Figure 1.10: Schematic illustration of RCSJ model and washboard potential. (a): Equivalent electrical circuit of RCSJ model. (b): Illustration of washboard potential. When $I < I_c$, the junction stays at the equilibrium (at the bottom of the potential). When $I > I_c$, however, the junction turns into a voltage state (escapes from the bottom of the potential).

1.3.3 FFLO state and Andreev bound state

As previously discussed, two superconductors can couple through a weak non-superconducting layer such as an insulator or a normal metal subject to the nonzero phase difference between the order parameters of two superconductors. This effect, called Josephson effect is mainly caused by the proximity effect of the superconductors. One van imagine the situation at the interface between superconductor and nonsuperconducting material such as a normal metal. Then Cooper pairs in superconductor can penetrate into the normal metal part within a certain length from the interface. In the view of the GL theory, this situation can be described as a finite value of the order parameter in the normal metal (see Fig. 1.11(a) and (b)). More microscopically, the BCS expression tells us that the proximity effect is explained by Andreev reflection [57, 58]. Assume a transparent interface between a superconductor and a normal metal (Fig. 1.11(c)). In transferring from a normal metal to a superconductor, one electron state cannot survive in the superconductor because it is in the condensate state unless the energy level of the electron is over the gap of the quasiparticle excitation. However, we can think another path for electrons entering into superconductor. This is the situation in which the electrons are converted into Cooper pairs through the interface. In order for this to occur, one electron has to find its partner. This partner is brought off the Fermi sea and can be regarded as a hole. This picture corresponds to the reflection of an incoming electron to a outgoing hole. This situation is therefore called the Andreev reflection.

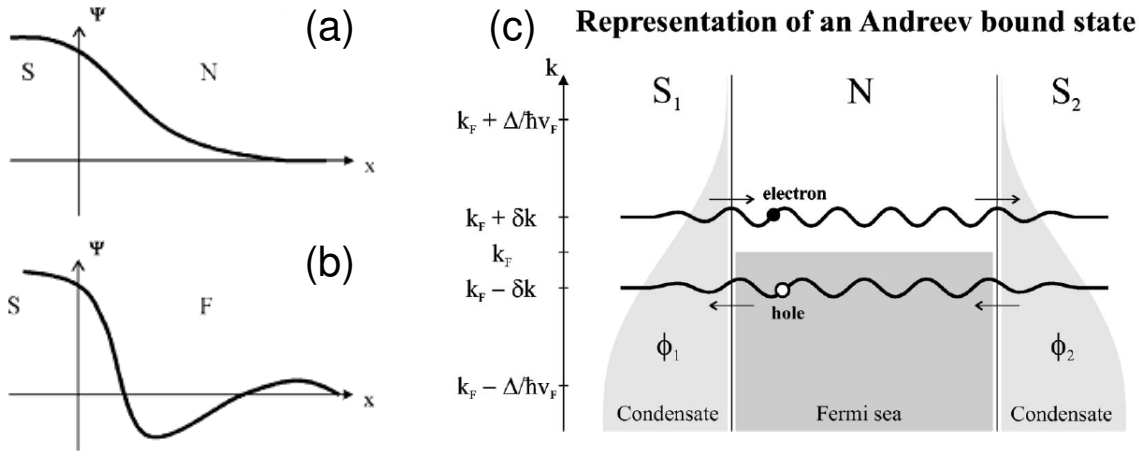

Figure 1.11: (a): Behavior of the superconducting order parameter at a S/N interface. It shows an exponential decay. (b): Behavior at a S/F interface. The order parameter oscillates as well as decays. (c): Schematic illustration of Andreev bound states [59]. Between two superconducting banks, an electron and a hole couple to make a bound state.

When there are two equivalent interfaces between superconductor and normal metal like in Josephson junction, the Andreev reflection induces an exotic phenomenon [59]. At the Fermi level, an electron and a hole correlated by the Andreev reflection have the same wave vector, $k_e = k_h$ and follow exactly the same path with the opposite group velocities. Therefore the relative phase of their wave function is constant through this path. As a result, the coherence length of the pair is very long (less than the phase coherence length). Imagine the situation in which the electron of the pair has a finite energy ϵ ($0 < \epsilon < \Delta$), where Δ denotes a gap of the superconductor. Due to this finite energy, the wave vector of the electron becomes

$$k_e = k_F + \frac{\epsilon}{\hbar v_F} \equiv k_F + \delta k. \tag{1.46}$$

Because another electron which pairs with the electron has the wave vector $k_F - \delta k$, the reflected hole also has the wave vector $k_h = k_F - \delta k$. Due to the difference in wave vector between the electron and the hole of $2\delta k$, this shifts the phase of the pair as $2\delta k x$ at a position x. This reduces the coherence length.

When two superconductors sandwich ferromagnet, the situation becomes different. Since in ferromagnet there are two spin subbands with the energy difference $2E_{\rm ex}$, where $E_{\rm ex}$ represents the exchange energy, an extra phase $q = \pm E_{\rm ex}/\hbar v_F$ is added according to the direction of spins. Considering the fact that in Andreev pair the electron and the hole are in different spin subbands, their wave vector now becomes

$$k_e^{\downarrow} = k_F - q + \delta k \tag{1.47}$$

$$k_h^{\uparrow} = k_F + q - \delta k \tag{1.48}$$

and

$$k_e^{\uparrow} = k_F + q + \delta k \tag{1.49}$$

$$k_h^{\downarrow} = k_F - q - \delta k. \tag{1.50}$$

At the Fermi level, namely, $\delta k = 0$, the Andreev pairs have a phase difference $2qx$ at a position x. This phase difference contributes to the shorter coherence length of the Cooper pair in ferromagnet. However, at a certain value of ϵ, which fulfills $q - \delta k = 0$, a long coherence is obtainable. In this regime, $\epsilon = E_{\mathrm{ex}}$ and the internal phase shift of the pair is compensated.

Next we consider another interface between a superconductor and a normal metal. Andreev reflection at the two interfaces creates bound states called "Andreev bound states". The condition for the bound states is that the relative phase difference between the paired electron and hole, $\varphi = \varphi_e - \varphi_h$, corresponds to the phase difference between two superconductors $\phi = \phi_1 - \phi_2$. In other cases, an incomplete phase difference φ which does not match ϕ is smeared out on average. Taking into account the extra phase from the evanescent part of the electron's(hole's) wave function in the superconductor, the condition for the Andreev bound state becomes

$$\varphi = 2\frac{\epsilon_n}{\hbar v_F} d = \pm\phi + 2\arccos\frac{\epsilon_n}{\Delta} + 2\pi n, \tag{1.51}$$

where d is the thickness of the normal metal and n is an integer. Each level is separated by $\pi \times \hbar v_F/d \equiv \pi E_{\mathrm{Th}}$.

When the normal metal part is ferromagnet, the condition changes due to the extra phase from the exchange energy E_{ex} in ferromagnet. The condition now becomes

$$\varphi = 2\frac{\epsilon_n \pm E_{\mathrm{ex}}}{\hbar v_F} d = \pm\phi + 2\arccos\frac{\epsilon_n}{\Delta} + 2\pi n. \tag{1.52}$$

In this situation we want to emphasize that the lowest bound state above the Fermi level, which most contributes to the transport property of the junction, is different in

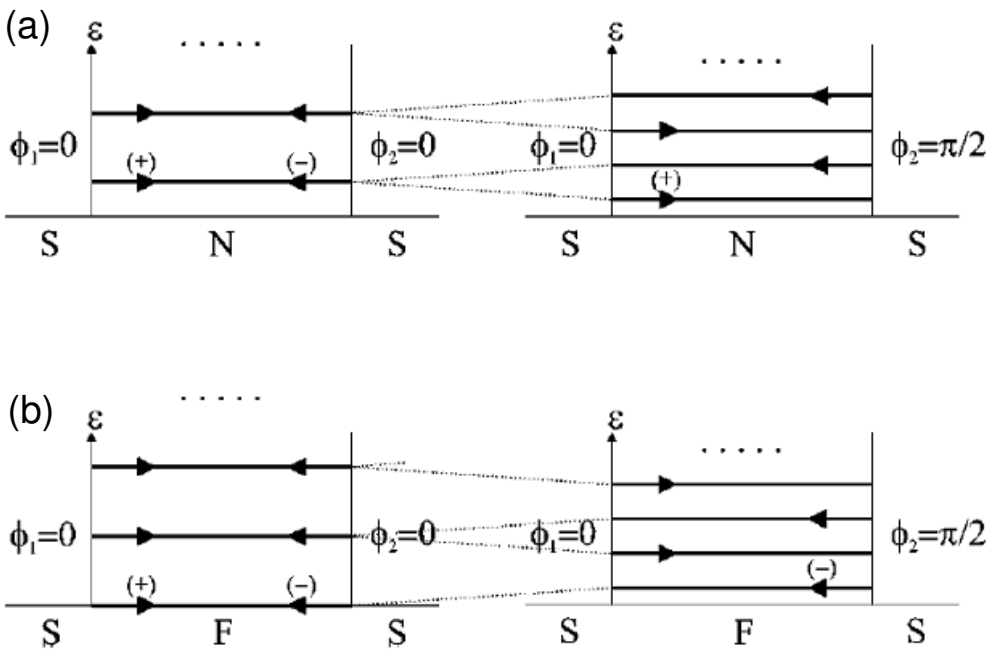

Figure 1.12: Andreev bound states in S/N/S junction (a) and S/F/S junction (b) [59]. (a): In S/N/S Josephson junction, (+) state and (-) state split when there is a phase difference of $\pi/2$. Since the level nearest the Fermi level is dominant in transport, supercurrent flows from left to right. (b): Due to the extra energy difference $E_{\rm ex}$, (-) state becomes dominant in S/F/S junction.

the S/N/S junction and the S/F/S junction as shown in Fig. 1.12. In the S/N/S junction, as $\epsilon = 0$ and $\phi = 0$ do not fulfill the bound state condition (1.51). Therefore the lowest bound state is above the Fermi level. On the other hand, in the S/F/S junction there can be a subband at the condition of $\epsilon = 0$ and $\phi = 0$. If there exists a phase difference between the two superconductors, the degeneracy from the two oppositely-directed supercurrent state is split. In the S/N/S junction, thus the lowest subband becomes (+) state. However, in the S/F/S junction, (+) state stays below the Fermi level even after the degeneracy is split. Therefore the lowest state above the Fermi level is (−) state. This difference in the direction of the supercurrent between S/N/S and S/F/S at a certain condition induces 0-π transition.

1.3.4 0-π transition

In the existence of an exchange field in a normal metal, 0-π transition can be observed in the Josephson junction. In the 0-π transition, the equilibrium phase difference between two superconductors changes from zero to π. The 0-π transition was theoretically predicted to occur in the S/F/S Josephson junction [60, 61, 62].

In experimental situation, we flow a bias current through the junction. Therefore

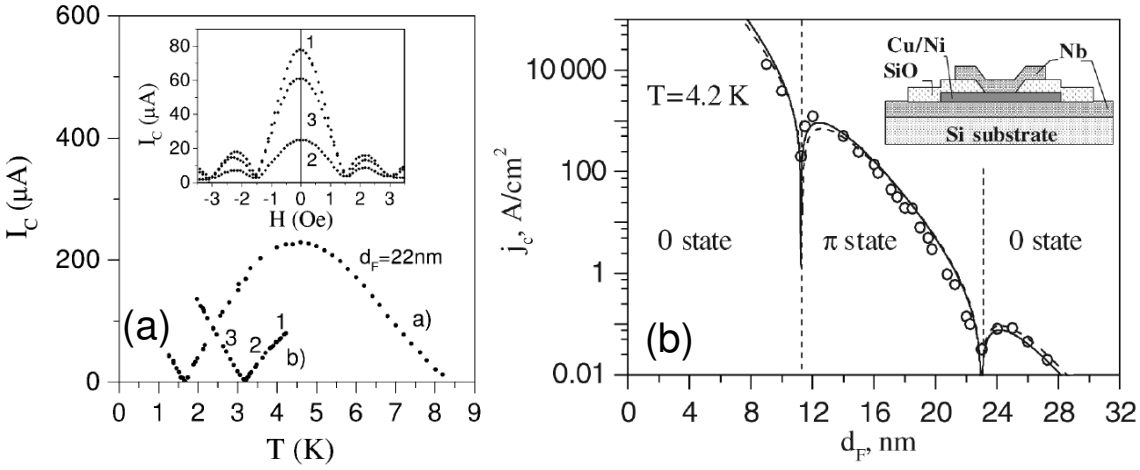

Figure 1.13: The results of the first two experiments of 0-π transition are shown. they modulated temperature of samples and thickness of F layer, respectively [62].

the relation between the supercurrent and the phase difference is

$$I = I_c \sin \varphi_0. \tag{1.53}$$

Here we ignore any other terms related to the junction's resistance and capacitance. If the equilibrium state becomes the π phase difference state, the relation changes

$$I = I_c \sin(\varphi_0 + \pi) = -I_c \sin \varphi_0. \tag{1.54}$$

This means that the direction of the supercurrent becomes opposite. As discussed in the last section, the 0-π transition derives from the spin subbands in ferromagnet. In the diffusive regime, this attributes to an oscillating behavior of the order parameter in ferromagnet: the coherence length of Cooper pair in ferromagnet can be expressed as

$$\frac{1}{\xi} = \frac{1}{\xi_1} + i\frac{1}{\xi_2} \tag{1.55}$$

$$\xi_{1.2} = \sqrt{\frac{\hbar D}{[E_{\text{ex}}^2 + (\pi kT)^2]^{1/2} \pm (kT)^2}}, \tag{1.56}$$

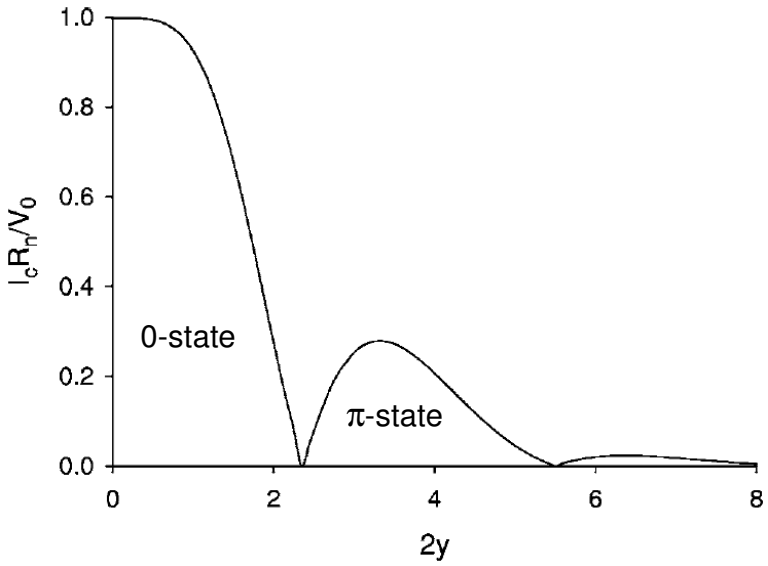

Figure 1.14: Relation between phase difference and layer thickness/coherence length of ferromagnet. Here $y = d_f/\xi_f$ [72]. Thus 0-π transition is induced both by the modulation of d_f and by ξ_f.

where ξ_1 takes + side and ξ_2 − side. As $\Psi \propto e^{-\frac{x}{\xi}}$, in ferromagnet $\Psi \propto e^{-\frac{x}{\xi_1}} \cos(\frac{x}{\xi_2})$. At an arbitrary condition, $\xi_1 < \xi_2$. Thus the oscillating behavior cannot be seen. However, especially when $E_{ex} \gg kT$, $\xi_1 > \xi_2$ is fulfilled and the oscillating behavior emerges. The oscillating behavior of the order parameter is shown in Fig. 1.11(b).

In spite of the intensive theoretical researches thereafter [63, 64], there have long been no experimental confirmations of the 0-π transition. In 2001, Ryazanov *et al.* first observed the 0-π transition by fabricating superconductor - ferromagnet - superconductor multilayer structures with CuNi as a ferromagnet (see Fig. 1.13) [65]. We note here that the condition for the oscillation is relevant to the thickness of the ferromagnet layer as well. As shown in Fig. 1.14, the equilibrium state of the S/F/S junction can be controlled by modulating either ξ_f or d_f, and they demonstrated the $0-\pi$ transition though the way of modulating the temperature of the sample (namely, ξ_f) and the thickness of the ferromagnet (d_f). These data were well reproduced by the theoretical calculations. Thereafter a large number of similar experiments were reported [66, 67, 68, 69]. However, there have been no clear experiments which prevail the relation between $E_{\rm ex}$ and the ground state of the junction. This is due to the impossibility to change the value of $E_{\rm ex}$ continuously. One should refer to [70] and [71] as a review of the recent research progresses about the ferromagnetic Josephson junction.

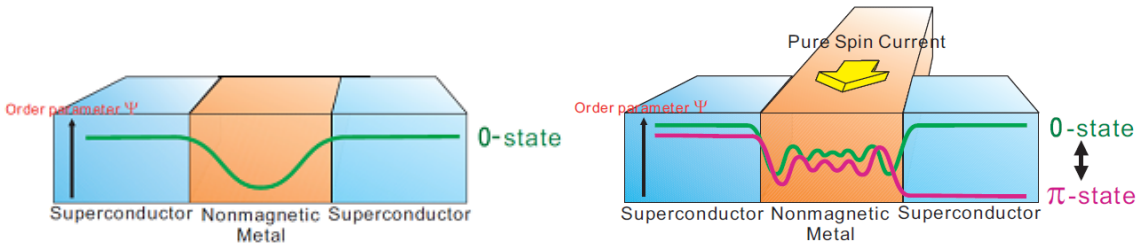

Ordinary S/N/S junction Spin injection into S/N/S junction

Figure 1.15: Schematic illustration of the spin injection into Josephson junction. (a) In an ordinary Josephson junction, the order parameter shows an exponential decrease. (b): Since the order parameter shows an oscillating behavior in S/F/S Josephson junction, the ground state changes from the 0 state to the π state according to the value of E_{ex}.

1.4 Scope of this thesis

As an next stage of spintronics, its application to some exotic physical phenomena is promising. In the last section of this chapter, we briefly mention motivations of our research and a structure of this thesis. Aiming to modulate physical phenomena through the spin current, we tried to control the ground state of the Josephson junction. The ground state of the Josephson junction with energy split(E_{ex}) between electron states with different spin directions becomes bistable in some condition as explained above. By modulating the amount of E_{ex}, the ground state changes from 0 to π phase difference (see Fig. 1.15). There have been no experiments which prevail the direct relation between E_{ex} and ground state. Thus the realization of the ground state control through E_{ex} modulation is of great importance.

However, it is essential to generate a spin current which has a large spin accumulation in order to see explicitly the effect of the spin current on a physical phenomenon itself. This is also the case for our experiments of the 0-π transition. Thus enhancing the spin accumulation is first to do. In our experiments, considering the application of the spin injection technique to the low temperature physics such as physics in the Josephson junction, we first tried to enhance the spin accumulation and then continued to the 0-π transition experiments.

In this thesis, we first show how to fabricate and measure the samples. We introduce these experimental processes both for the spin accumulation enhancement experiments and for the spin injection into the Josephson junction experiments. In the next chapter, we show the results of the spin accumulation enhancement experiments. Fortunately, we could obtain larger signals both at 10 K and at room temperature. The enhanced signals are expected to become much larger at 350 mK, in which we perform the 0-π

transition experiments. Our technique for the enhancement is to insert an insulating layer (MgO) between F and N. This insulating layer compensates the spin resistance mismatch and enhance the spin accumulation signal when its thickness is appropriately modulated. Then we continued to apply it to the spin injection into Josephson junction experiments. Finally, we show a summary and a conclusion of the results and discuss future work.

Our results of the spin injection experiments are suggestive to the application of the spin injection technique to physical phenomena at low temperatures. As we mention lastly, a suppression of heat effects is one of the key points to the application. In a decade there are some theoretical proposals to the application of the spin injection to other physical phenomena [72, 73]. Realization of these applications is invaluable and opens a new phase for spintronics.

Chapter 2

Experimental methods

2.1 Sample fabrication

In this chapter we briefly introduce the details of the sample fabrication and measurement.

2.1.1 Electron-beam lithography and Liftoff process

Mesoscopic physics including spintronics has developed with the progress of nanofabrication technique. Electron beam(EB) lithography is one of the representatives essential to fabricate nanoscale samples. By using the high energy electron beam, it has a much higher resolution than that of the optical lithography. Therefore we can design a nanoscale pattern created by a CAD computer program and precisely copy it by using the EB lithography onto a substrate.

All samples we measured were patterned by the EB lithography on an electron-sensitive resist. After the lithography, we deposit materials in order to construct the sample structures. The deposition was performed in several ways according to the materials: the EB evaporation, the resistive evaporation and the magnetron sputtering. In this subsection, we briefly show the sample fabrication process.

We first explain the EB lithography technique. The EB lithography is used for pattering the fine pattern onto the substrate coated with the electron-sensitive resists. In the EB lithography process, a part of the resist on the substrate is exposed to an electron beam to the pattern we designed. The exposed part is chemically deformed. Since this chemical deformation changes the sensitivity of the resist to the chemical solution (developer), the patterned part is selectively developed in a chemical solution.

Before the lithography, we prepare a substrate coated with a layer of a resist. All of the substrates we used are the thermally oxidized silicon(Si/SiO_2) substrate. First we coat a substrate with a resist. As a resist, we use two types; polymethylmethacrylate(PMMA) resist and methyl methacrylate(MMA) resist. They have a dif-

ferent sensitivity to the electron beam. Conventionally, we only use the PMMA resist for the lithography. However, in order to deposit several materials *in situ*, for the shadow evaporation process we coat both the PMMA and the MMA resists. Due to the difference of the sensitivity to the electron beam, the layers of the resists have an undercut structure. We can thus deposit different materials at different angles. The details are explained below.

The resists are coated by a conventional spin coater. The conditions for coating are shown in the table below.

Resist	Material/Process	Rotation number/Time (s)
PMMA	Cu	3000/60
PMMA	Py,Nb	4000/60
PMMA	shadow evap.	5000/60
MMA	shadow evap.	3000/60

After coating the resist, we next anneal the sample on a conventional baker. Annealing condition is summarized in the table below.

Resist	Annealing time/Temperature
PMMA	5 min/180 °C
MMA in PMMA/MMA	3 min/180 °C
PMMA in PMMA/MMA	5 min/180 °C

Next the process continues to the EB lithography. In our fabrication, we use the "Elionix6600 electron beam lithography system" for the EB lithography. The patterns are created as a CAD file. In the EB lithography process, a part of the resist on the substrate is exposed to an electron beam according to the pattern we designed. After the exposition to a high energy electron beam, that part is chemically deformed. Since this chemical deformation changes the sensitivity of the resist to the chemical solution (called developer), the patterned part is selectively developed in a chemical solution.

Acceleration voltage is 75 kV for all conditions. One refers the other conditions for the lithography to the table below

Resist	Emission current	Dose time
PMMA (Fine pattern)	400 pA	2.1 μs
PMMA (Coarse pattern)	1 nA	0.8 μs
PMMA/MMA double-layer resist (Fine pattern)	440 pA	2.2 μs
PMMA/MMA double-layer resist (Coarse pattern)	4.0 $\sim$ 4.4 nA	0.22 μs

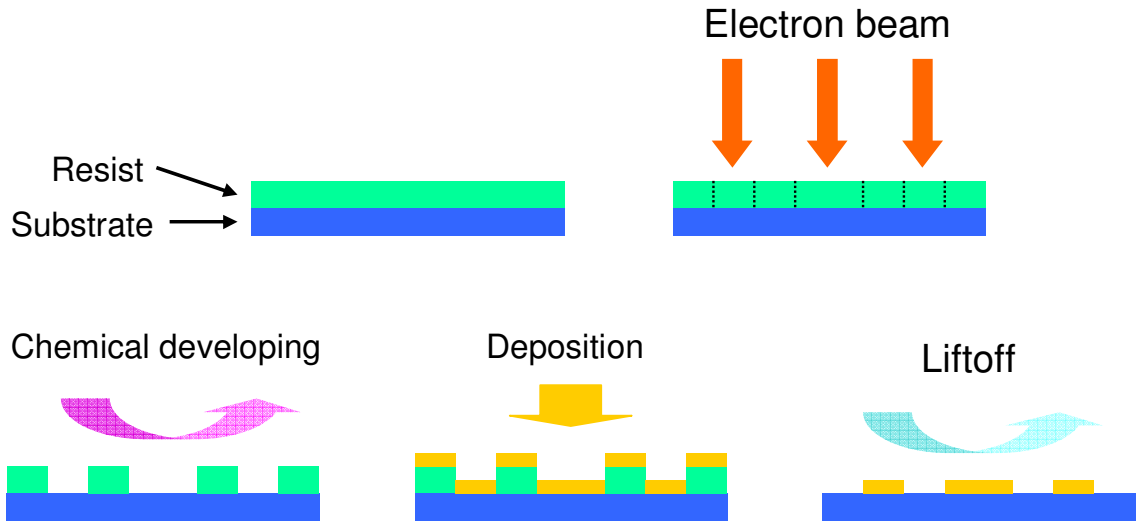

Figure 2.1: Sequence of the sample fabrication process by liftoff technique. (a): Resist is coated on the substrate. (b): The substrate is exposed to the EB, and the exposed area is chemically deformed. (c): Using the chemical solution, the exposed area is selectively developed. (d): A material is deposited onto the substrate. It is on the substrate only through the exposed area. (e): The remaining resist is lift off by the chemical solution and the material remains according to the pattern.

After patterning, the substrate is developed. As a developer, we use a chemical solution composed of MIBK and IPA with the ratio of 4:1. The developing time is 30 s.

The next step is the deposition of materials. For our samples, the deposited materials are Nb, Py, Cu and MgO. Nb and Py are deposited through the EB evaporation technique. In depositing Cu, we used the resistive evaporation technique. The difference of the deposition technique is mainly due to the difference of the evaporation temperature of each metal. MgO is an insulator and sputtered by the magneto-sputtering (see below). Except samples fabricated by the shadow evaporation technique, these metals are deposited normal to the substrate. The thickness of these materials are the same for all samples. See the table for checking the deposition condition and the thickness of each material.

Material	Deposition rate	Thickness
Cu	2.0 $\sim$ 4.0 Å/s	100 nm
Py	0.4 $\sim$ 1.5 Å/s	20 nm
Nb	2.5 $\sim$ 4.0 Å/s	30 nm

After the deposition the substrate is dipped in the chemical solution for more than two hours for liftoff. The resist dissolves in the solution and extra parts of the metallic layers on it are lift off the substrate. Only the patterned area with metallic layers

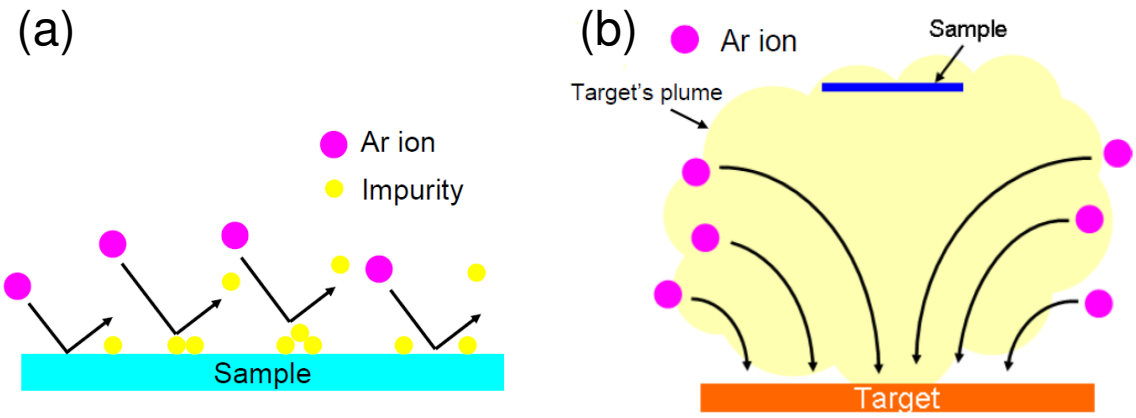

Figure 2.2: Schematic illustration of milling (a) and sputtering (b). (a): Ar gas is ionized by a high electric field. Accelerated Ar ions collide with the impurities on the substrate and wash them up. (b): Ionized Ar is induced to collide with the target material by the cyclotron motion. The target is evaporated to the substrate.

therefore still remains. All procedures in the process are illustrated in Fig. 2.1. This process is called "lift-off" process named after the procedure we mentioned above and in this way, the nanoscale metallic structure is constructed.

In the real fabrication procedure, we have to deposit several kinds of material. Because the sample is exposed to the atmosphere between the subsequent deposition, the surface to which the next material is deposited has to be cleaned up for ruling out spurious effects: there are some possibilities to have some impurities or some oxidized materials of the surface. As a technique for removing such impurities or oxidized materials, we perform Ar-ion milling before the deposition. In the milling process Ar gas is ionized by high electric field and then accelerated to the surface of the sample. As a result the impurities or oxidized materials are washed up by the Ar ions. Milling is performed under 2×10^{-4} Pa, and the beam current and the acceleration voltage are 12 mA and 600 V, respectively.

Ar ion is also used for depositing some materials in the magnetron sputtering technique. Sputtering technique is used for fabricating a thin film of metals or oxides. Ar is ionized by the high electric field and the ionized Ar is induced to the surface of a target by a magnetic field to generate a plume of the target. In our fabrication, MgO layer is deposited by sputtering. the mechanism of the Ar ion milling and the magneto-sputtering are illustrated in Fig. 2.2.

At the end of the fabrication we deposit alumina(Al_2O_3) on the overall substrate in order to prevent the oxidization of the surface of metals. Alumina is also sputtered by the magnetron sputtering technique.

2.1.2 Shadow evaporation technique

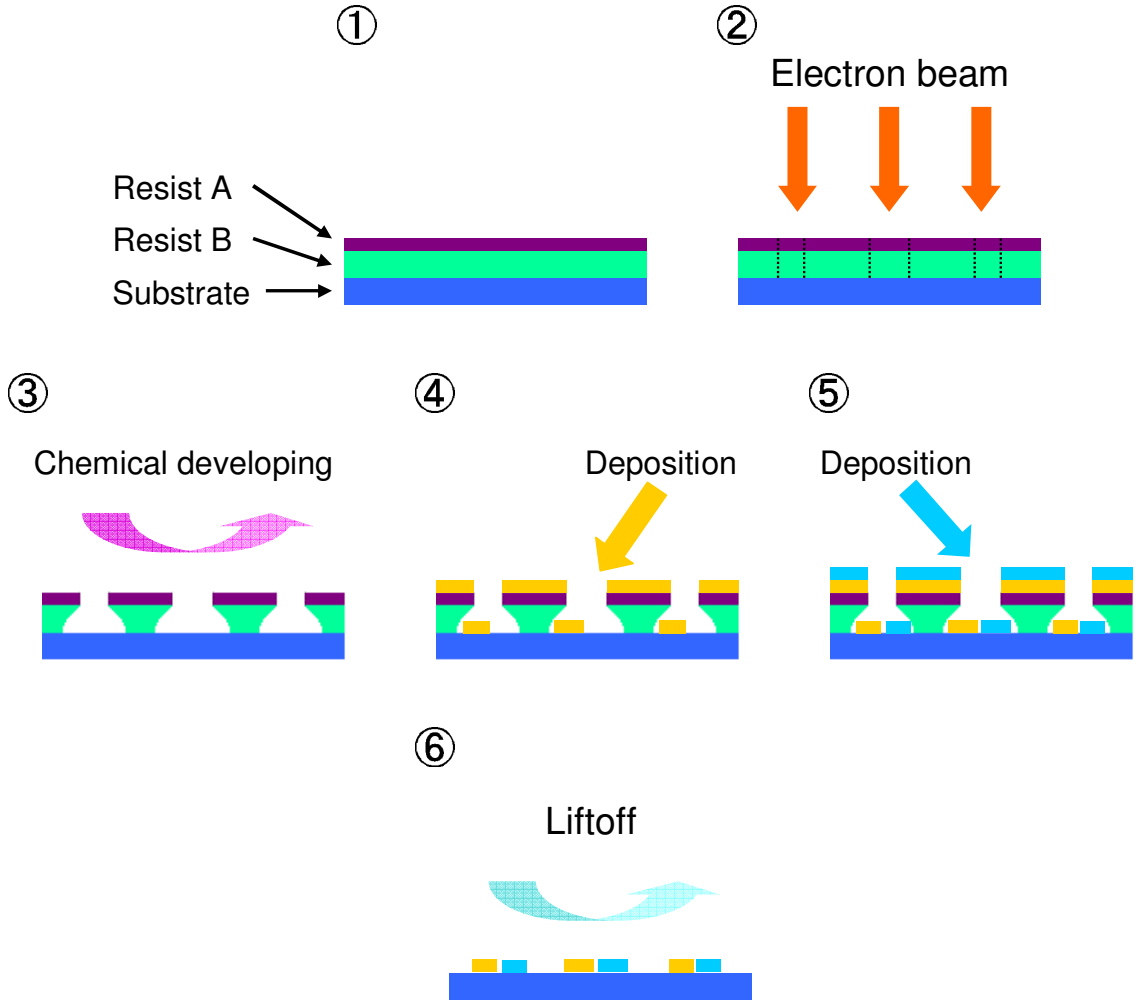

Figure 2.3: Sequence of the shadow evaporation technique. (a): Two different resists are coated on top of the substrate. (b): The resists are exposed to the electron beam. (c): Since the sensitivity to the developer is different between the two resists, the lower resist is overdeveloped and transversal area has a trapezoid shape. (d,e): By depositing different materials at different angles, it is possible to deposit different kinds of material. (f): The resists are lift off at a time.

We introduced the conventional sample fabrication technique above. However, this process has a disadvantage in that for depositing many layers of metals, we have to do the procedure one by one. This sometimes causes the contamination of the interface between different materials even if we perform milling. In our structures, the transport of electrons between different materials such as ferromagnet and nonmagnetic metal, or superconductor and nonmagnetic metal is a key issue. Therefore, it is preferable to keep the interface between these materials transparent. As explained below, we have another fabrication technique for keeping the interface transparent, which is called

"shadow evaporation technique". This technique is prior to the surface cleaning by the Ar ion milling in making good contacts.

Using the shadow evaporation technique, one can deposit subsequently different kinds of material *in situ* at different angles. for the shadow evaporation, we have to prepare two different types of resist which have different sensitivities to the chemical solutions: polymethyl-methacrylate(PMMA) and methacrylate(MMA). After developing, due to the difference of the sensitivity, we have an undercut structure (see Fig. 2.3). Therefore, the exposed area of the substrate is nominally larger compared with that of the substrate patterned with the usual single layer (e.g. PMMA) resist. Due to this "*trapezoid*" shape of the transversal area of the resist, we can deposit different kinds of material *in situ* at different angles toward the substrate.

As an example, we introduce the fabrication of the samples for the spin injection into the Josephson junction. First we deposit Nb at an angle of 30° toward the vertical axis of the substrate. Then we transversely rotate the sample by 90°, and then deposit Py at an angle of 60°. After depositing these two materials, we finally deposit Cu normal to the substrate. Through this procedure, we can fabricate the samples *in situ* and thus keep the interface between different materials clean. We use this shadow evaporation technique for the fabrication of the NLSV structure and the Josephson junction.

2.2 Measurements

We perform the electrical measurements both at room temperature (RT) and at low temperature. In the NLSV measurements, the samples are cooled down to 10 K. In the experiments of the spin injection into the Josephson junction, the samples are measured at 350 mK. A magnetic field is applied to the sample by the solenoid magnet in NLSV experiments. Details are explained below.

2.2.1 Measurement circuits

A schematic illustration of the measurement circuits are shown in Fig. 2.4. We use a conventional four-point ac rock-in technique for electrical measurements of the NLSV signals with the frequency of 173 Hz. The detected signals are averaged in one to three seconds according to the temperature.

In the measurements of the spin injection to the Josephson junction, we add a trans to the electrical circuit based on the previous one. The trans is for biasing a ac current to the junction with a small step. A dc current source is also used for the spin injection current. In both experiments, the signals are amplified to 1000 times to the detected value.

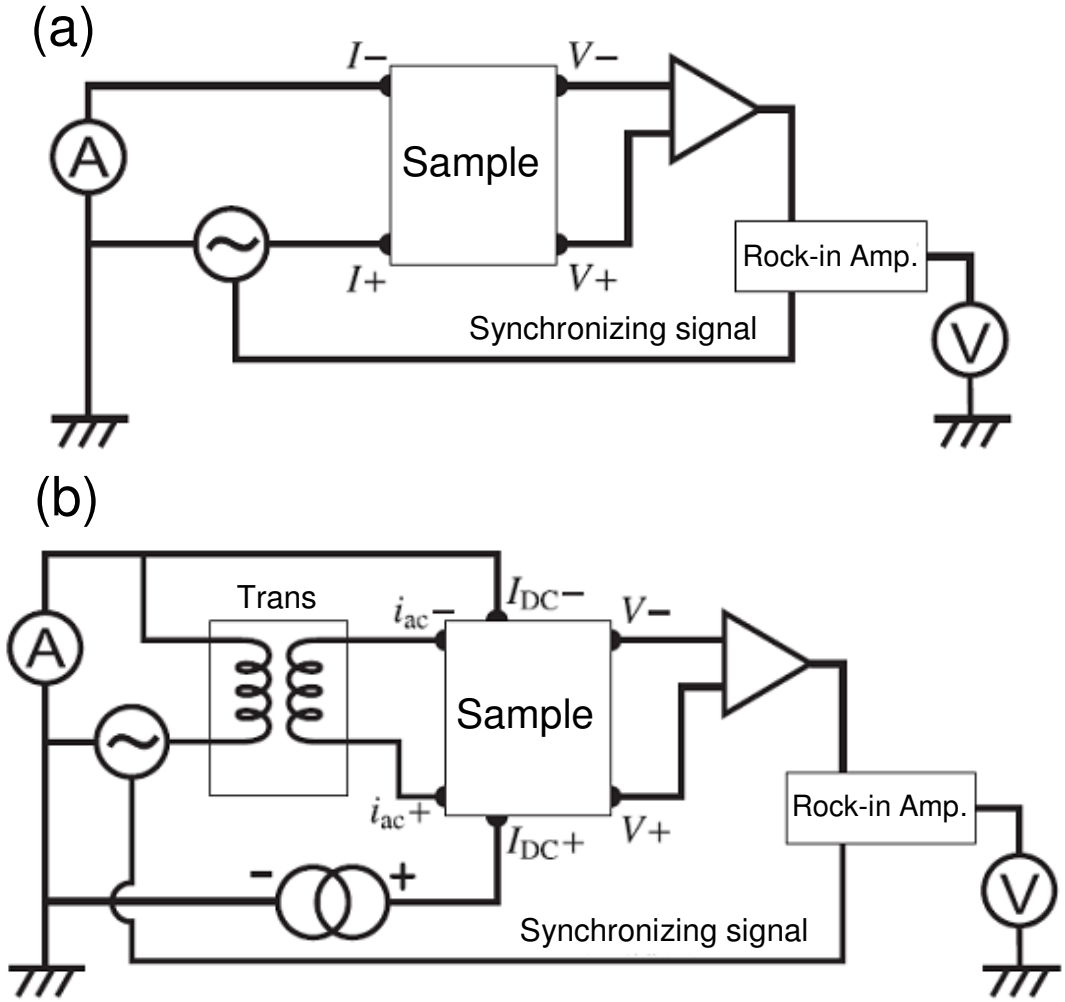

Figure 2.4: Schematic illustration of the circuit for electrical measurements. (a): Electrical circuit for all measurements except the Josephson junction measurements. (b): Electrical circuit for the Josephson junction measurements.

2.2.2 Cooling system

We measured the samples at both RT and low temperatures. Fig. 2.5 shows our cooling system. The samples for the NLSV measurements are cooled down to 10 K, using ^{4}He flow cryostat. In this system, a sample is directly exposed to the flowing ^{4}He gas pumped from the vessel which contained ^{4}He. The temperature is well controlled by the feedback method with an external heater. In the Josephson junction experiments, we use a one-shot ^{3}He cryostat. Sample is now in the inner vacuum can(IVC), a cylinder which encloses the sample holder. First IVC is pumped up to an order of 1×10^{-3} Pa through a fine vessel along the sample rod. Next ^{4}He exchange gas is injected into IVC for absorbing heat in exchange with the outer flowing ^{4}He gas. In this way, the sample is cooled down to $T < 10$ K. Then IVC is again pumped and simultaneously ^{3}He gas

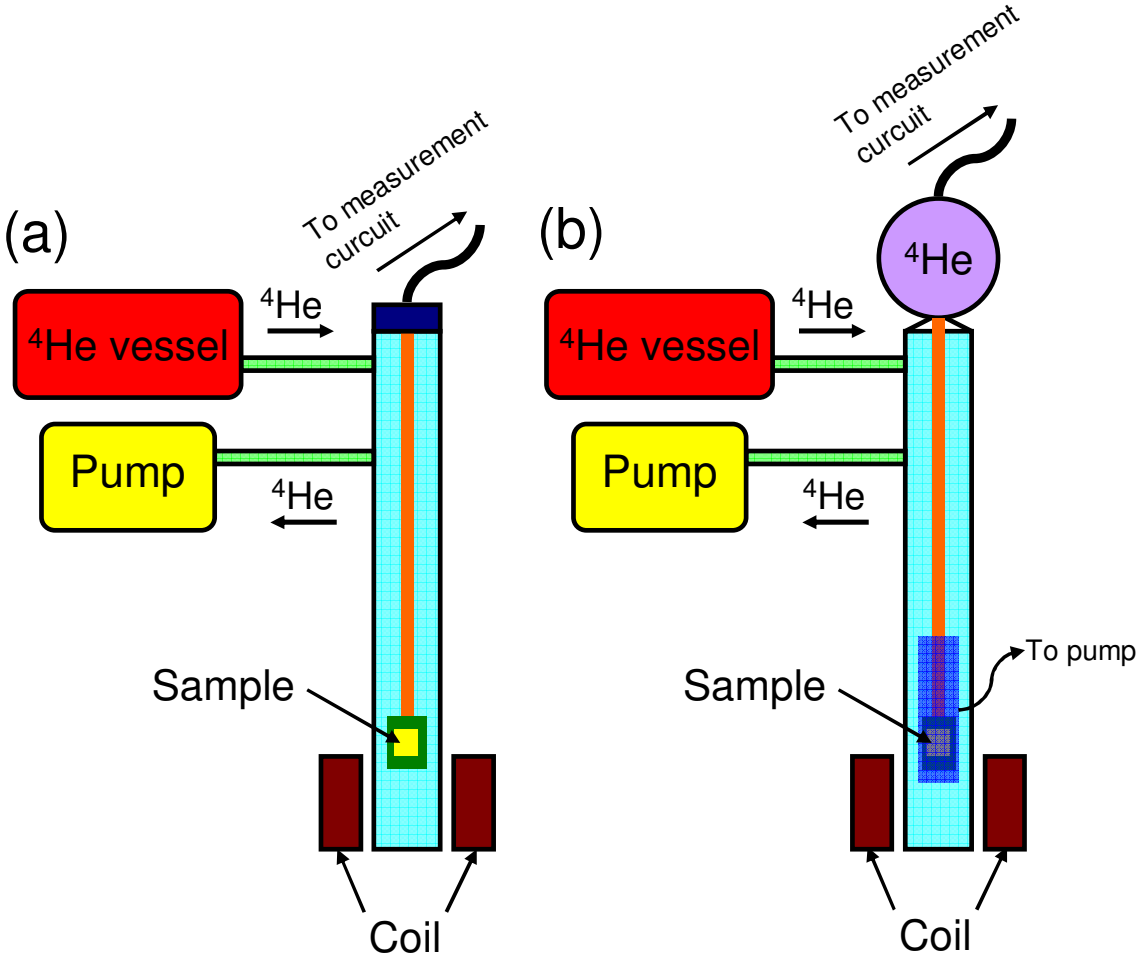

Figure 2.5: Schematic illustration of cooling system. (a): ^{4}He flow cooling system. A sample is exposed to a flowing ^{4}He gas and is cooled down to 10 K. (b): One shot ^{3}He cryostat. A sample in now in IVC and is cooled down to 350 mK.

contained in the pot on the top of the sample rod is condensed. After the condensation is completed, the absorption pump will start to cool the pot and the sample down to 350 mK. The cooling is kept at for seven hours.

Chapter 3

Spin Accumulation Enhancement

3.1 Motivation

An efficient spin injection into nonmagnetic metals is one of the key issues in spintronics. When Johnson and Silsbee first demonstrated the spin injection into Al, the value of the spin accumulation (namely, ΔV) was only an order of picovolt and the spin polarization was 0.06 at $T = 4.3$ K [19]. After the early stage of the spin injection experiments, several theoretical calculations pointed out that the *conductivity mismatch* prevents the efficient spin injection [43, 44]. In the spin injection into semiconductors, for example, there is a resistance mismatch between ferromagnet and semiconductor. Due to this mismatch, the spin injection efficiency becomes quite small. In order to attain the spin injection into semiconductors, magnetic semiconductors are therefore now widely used for the spin injector instead of metal. For the spin injection into metals, a resistive interface between the spin injector and nonmagnet was predicted to enhance the spin injection efficiency: by inserting an insulating layer between the spin injector/detector and the nonmagnetic metal, the insulating layer behaves as a spin filter and the efficiency of the spin injection increases. Some of these theoretical predictions were experimentally demonstrated [45, 46].

The efficiency of the spin injection is often described by the spin polarization of the injected electrons. However, in order to apply the spin injection technique to other physical phenomena relevant to the magnetism, the value of the spin accumulation signal is more important than the spin polarization. In this section, we show how to enhance the spin accumulation in Py/Cu/Py NLSV structures. Our motivation is to apply the technique we obtained here to the research for the ground state control of the Josephson junction by the spin current. In our experiments we thus put emphasis on the enhancement of the spin accumulation rather than the spin polarization.

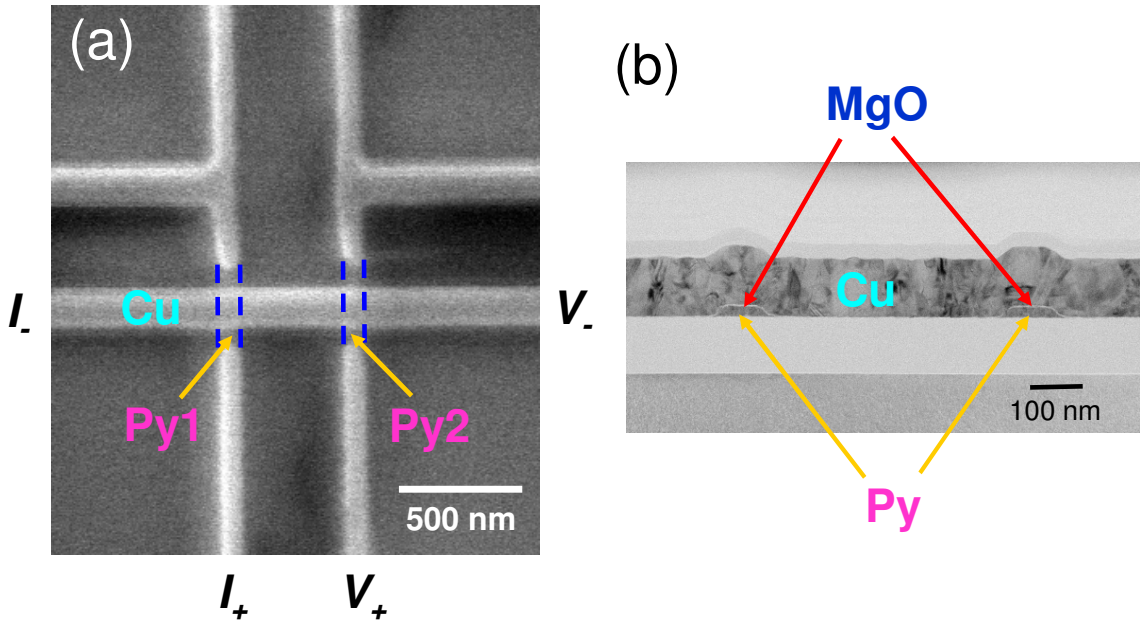

Figure 3.1: (a): SEM image of a NLSV sample fabricated under the shadow evaporation technique. Two Py wires are bridged by Cu strip. (b) TEM image of a transversal area of the sample. We can clearly see the inserted MgO layer between Py and Cu.

3.2 Sample structure and fabrication

Our samples have a typical NLSV structure. A scanning electron microscope (SEM) image of a sample is shown in Fig. 3.1(a). In order to flip the magnetization of the two ferromagnet strips independently, one of them has a large pad at its edge (not shown in Fig. 3.1(a)). As a ferromagnet (F), we use Py for the lack of a crystal magnetic anisotropy. As a result, F has only a shape anisotropy. The small rectangular shape ensures that the magnetization of Py is along the longitudinal axis of the wires and in a single domain. A nonmagnet (N) wire, Cu, bridges the two F strips. In order to create the resistive interface between F and N for obtaining an efficient spin injection, we inserted the MgO layer between Py and Cu. The MgO layer works as an insulator because it is both theoretically and experimentally proved that the MgO layer is one of the best spin filtering insulators through the many TMR experiments [9]. For fabricating the interface between these materials without any spurious effects, we used the shadow evaporation technique introduced in the previous section. Py was evaporated by the EB evaporation onto the substrate at an angle of 60° measured by the perpendicular axis of the substrate. Next the sample was transferred to another chamber. After filling the chamber with the Ar gas, MgO was sputtered onto the Py wire using the magneto-sputtering technique. The sputtering was performed under the condition of 1.4×10^{-1} Pa and the sputtering power was kept at 20 W. By changing the

sputtering time, we controlled the thickness of the deposited the MgO layer. Finally, the sample was again moved to the other chamber and Cu was deposited by using the resistive evaporation normal to the substrate. As a final treatment the entire substrate is covered with alumina in case that the surface of the sample is oxidized. The center-to-center distance between the two F strips were changed between 300 nm and 1100 nm. This is mainly for investigating the distance dependence of the NLSV signals. The width of the two materials was fixed to 100 nm and 200 nm. Although the thickness of the MgO layer was not accurately measured, we confirmed through the tunnel electron microscope (TEM) image that one of the sample with the interface resistance $3.0 \times 10^{-1}\Omega(\mathrm{cm})^2$ had around 1 nm-thick MgO layer (see Fig. 3.1(b)).

3.3 Measurements and Results

Measurements were performed both at RT and 10 K. For electrical measurements including the detection of NLSV signals and the interface resistance, we used the rock-in technique explained in the previous chapter. The configuration of the electrodes in the NLSV experiments is shown in the SEM image of the sample (Fig. 3.1(a)). During the NLSV measurements, an external magnetic field was swept along the easy (magnetization) axis of the Py strips. The bias current was fixed to 90 μA at both temperatures. Depending on the relative direction of the magnetization between the two Py strips, the detected voltage normalized by the bias current show the typical NLSV signals (one of them is shown in Fig. 3.2). The spin accumulation $\Delta R = \Delta V/I$ is defined as the difference in V/I between two magnetization configurations (parallel or antiparallel).

We first measured the NLSV samples with Ohmic F/N junctions and different center-to-center distances between the two Py wires (d), in order to determine several physical parameters such as the spin diffusion length of N (λ_{N}) and the spin polarization of Py (P_{F}). d was varied from 300 to 900 nm. The data at 10 K are shown in Fig. 3.4. Since the shape of the Py strips has some scatters due to the fabrication process, there is an asymmetry of the switching fields between the two Py strips. Thus some samples did not show the symmetric NLSV signal (see Fig. 3.3).

The relation between the distance (d) of the two Py wires and the spin accumulation can be described as below [41]:

$$\Delta R = 4R_{\mathrm{SN}} \frac{\left(P_{\mathrm{I}}\frac{R_{\mathrm{SI}}}{R_{\mathrm{SN}}} + P_{\mathrm{F}}\frac{R_{\mathrm{SF}}}{R_{\mathrm{SN}}}\right)^2 e^{-d/\lambda_{\mathrm{N}}}}{\left(1 + 2\frac{R_{\mathrm{SI}}}{R_{\mathrm{SN}}} + 2\frac{R_{\mathrm{SF}}}{R_{\mathrm{SN}}}\right)^2 - e^{-2d/\lambda_{\mathrm{N}}}}, \tag{3.1}$$

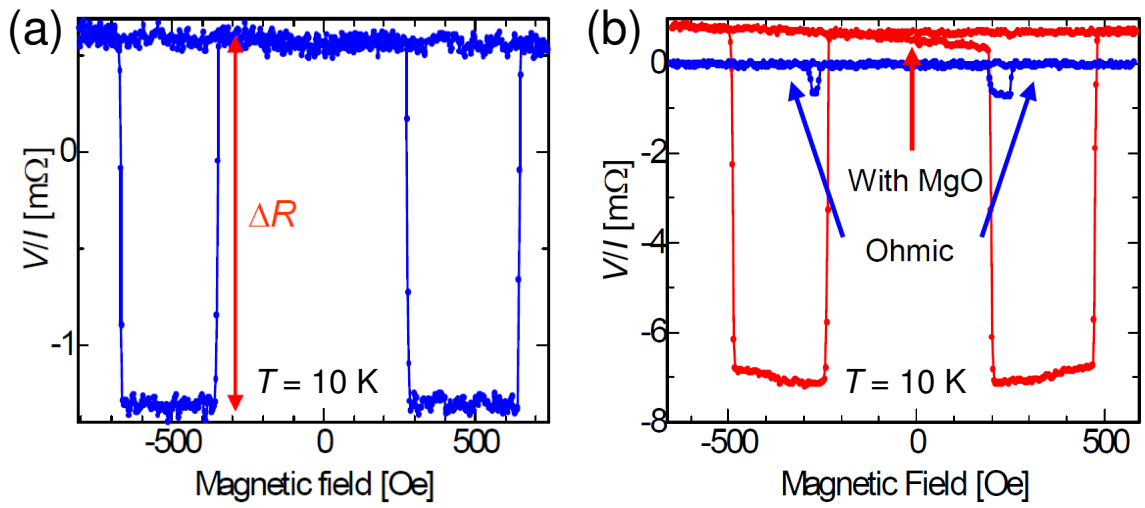

Figure 3.2: (a)Typical NLSV signals from the sample with Ohmic Py/Cu contact. ΔR is defined as the difference in V/I of parallel and antiparallel magnetization state. (b) Comparison of the NLSV signals in the samples with/without MgO layer at 10 K. The signal is explicitly enhanced by the insertion of the MgO layer.

where

$$R_{\mathrm{SN}} = \frac{\rho_{\mathrm{N}}\lambda_{\mathrm{N}}}{t_{\mathrm{N}}w_{\mathrm{N}}}, \tag{3.2}$$

$$R_{\mathrm{SF}} = \frac{\rho_{\mathrm{F}}\lambda_{\mathrm{F}}}{w_{\mathrm{F}}w_{\mathrm{N}}(1-P_{\mathrm{F}}^2)} \tag{3.3}$$

and

$$R_{\mathrm{SI}} = \frac{R_{\mathrm{I}}}{w_{\mathrm{F}}w_{\mathrm{N}}(1-P_{\mathrm{I}}^2)} \tag{3.4}$$

are the spin resistances (see the Chapter 1) of Cu (nonmagnetic), Py (ferromagnetic), and an interface, respectively. P_{I} stands for the spin polarization of the interface. ρ_{X} is the resistivity, t_{X} the thickness, and w_{X} the width of material X (N or F).

By substituting $R_{\mathrm{I}} = 0$ and $P_{\mathrm{I}} = 0$ for Ohmic contacts between F and N in the Eq. (3.1), we can experimentally obtainthe unknown parameters shown below

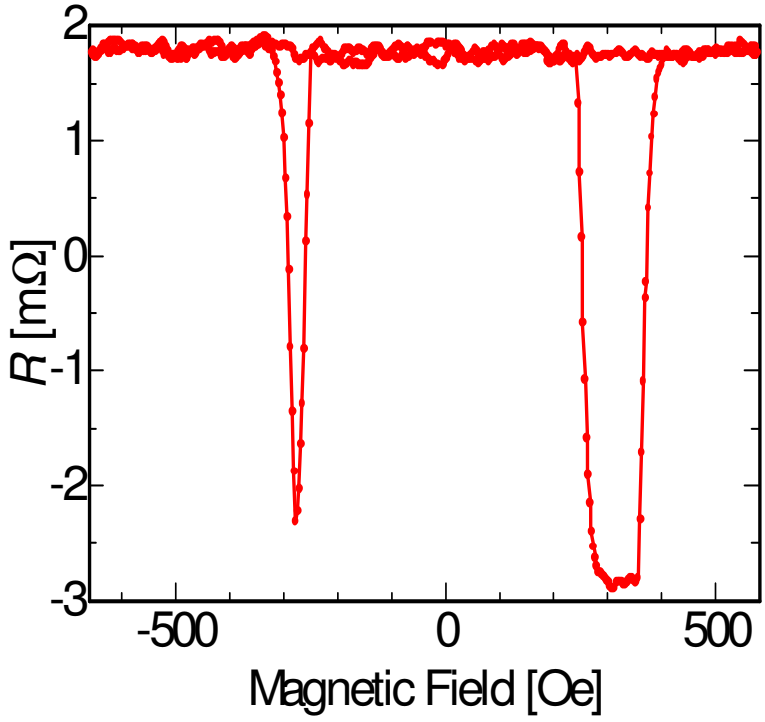

Figure 3.3: Typical symmetric NLSV signal. In this situation, we take ΔR as the larger difference in R between parallel/antiparallel magnetization configuration.

Parameter	Value (10 K)	Value (RT)
P_{I}	0.11	0.11
P_{F}	0.26	null
λ_{N}	1.3 μm	550 nm
λ_{F}	5 nm	5 nm

Here we note that the spin diffusion length of Cu (λ_{N}) reaches 1.3 μm at 10 K. We assume that the spin diffusion length of Py (λ_{F}) is fixed to 5 nm both at 10 K and at RT from our previous studies. This value is twice larger than the value previously obtained in the Py/Ag/Py NLSVs [45]. If we consider the application of the spin injection technique to the modulation of the Josephson junction, a longer spin diffusion length is more preferable since the effective magnetic field on the junction become more homogeneous.

We also measured the NLSV samples with the MgO layer between F and N. By inserting the MgO layer, one can enhance the spin injection efficiency. For Ohmic contacts, the interface resistance sometimes shows negative values. This is because of the inhomogeneity of a current at the interface. This inhomogeneity becomes negligible if the interface resistance is higher [42]. We measured many samples with different

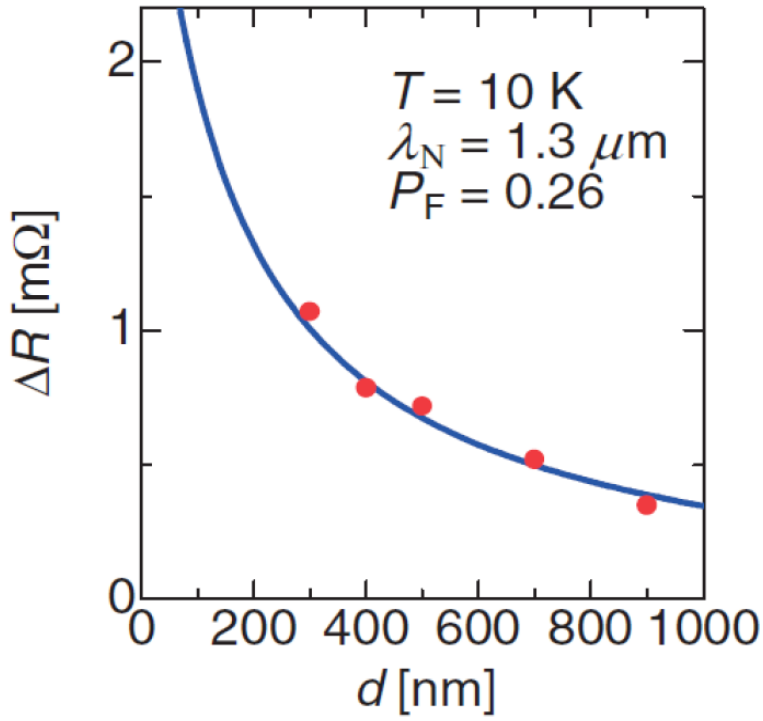

Figure 3.4: Distance dependence of the spin accumulation signal obtained at 10 K. Solid curve is obtained from the theoretical equation. Data points are well fit to the theoretical curve.

interface resistances and investigated the relation between the interface resistance and the spin accumulation signal. In this experiment, the interface resistance of the two Py/Cu junctions (the injector and the detector) was not always the same value. Thus we selected the samples whose interface resistances showed a deviation within 20 % of the value themselves. For determining the interface resistance of such samples, we averaged the two values of the interface resistance.

We next plot the spin accumulation signal as a function of the interface resistance measured at 10 K and at RT (Fig. 3.5). With increasing interface resistance (R_{I}) changes, the spin accumulation signal ΔR shows a dramatic change: ΔR rapidly increases until R_{I} reaches a certain value (3.0×10^{-1} $\Omega(\mathrm{cm})^2$ at 10 K, 2.0×10^{-1} $\Omega(\mathrm{cm})^2$ at RT) and then suddenly decreases.

By modulating the interface resistance, we obtained $\Delta R = 10$ mΩ in the sample with $d = 300$ nm and $R_{\mathrm{I}} = 3.0 \times 10^{-1}$ $\Omega(\mathrm{cm})^2$ at 10 K. The spin accumulation voltages reached ~ 10 μV with a current $I \sim 1$ mA. This value is about ten times larger than that obtained from the NLSVs with the Ohmic contact. Thus the data verify that the insertion of the MgO layer enables the enhancement of the spin accumulation.

We also measured the R_{I} dependence of ΔR for $d = 500$ nm and $d = 700$ nm. All samples showed the same tendency: as the interface resistance, the spin accumulation

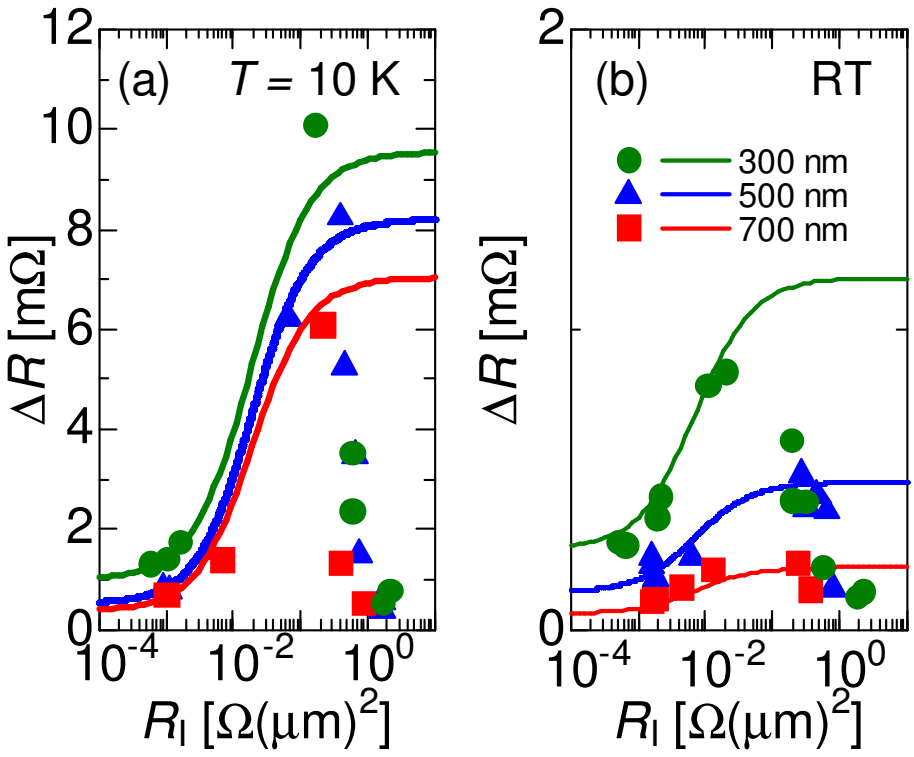

Figure 3.5: Relation between the interface resistance and the spin accumulation signal. The distance between two Pys is 300, 500, and 700 nm. When $R_{\mathrm{I}} < R_{\mathrm{I}}^{\mathrm{max}}$, data are well fit to the theoretical curves.

first increases and then suddenly decreases. The value of the interface resistance where the spin accumulation signal has its maximum ($R_{\mathrm{I}}^{\mathrm{max}}$ is almost the same for the different d samples. This implies that $R_{\mathrm{I}}^{\mathrm{max}}$ has some physical meaning.

3.4 Discussions

We next discuss how to interpret the data. We use Eq. (3.1) to explain the data and treat R_{I} and P_{I} as variable parameters due to the MgO layer at the interface. We can determine some parameters including P_{I} from the experimental data. They are shown in the table below.

Parameter	Value (10 K)	Value (RT)
P_{I}	0.11	0.11
P_{F}	0.26	null
λ_{N}	1.3 μm	null
λ_{F}	5 nm	5 nm

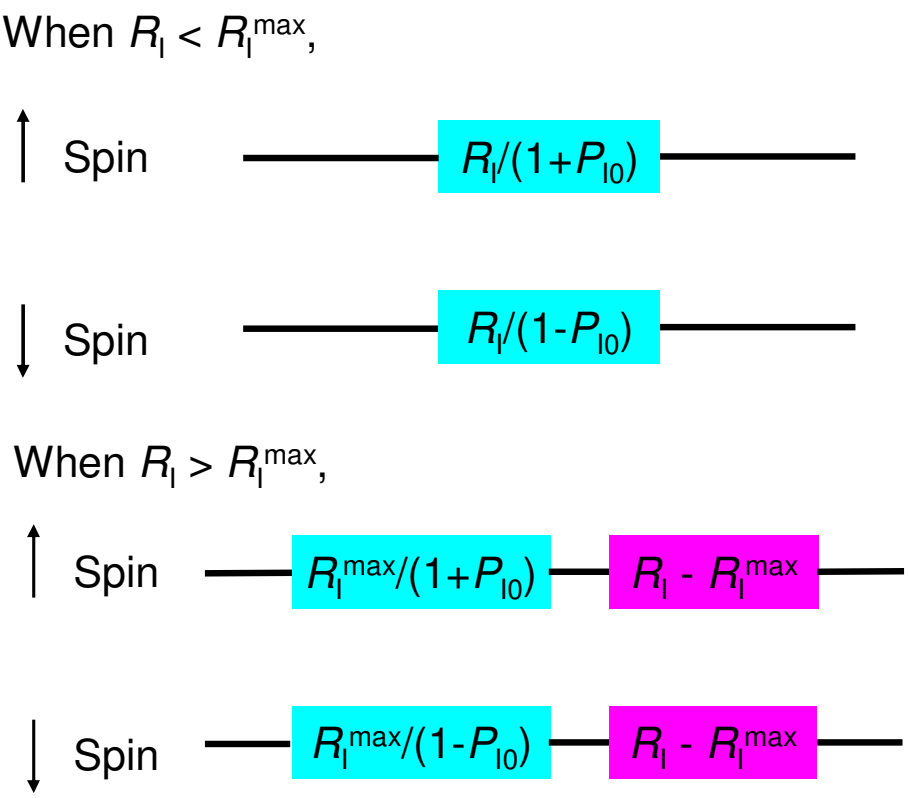

Figure 3.6: Schematic illustration of the modified model. When $R_{\rm I} < R_{\rm I}^{\rm max}$ the two channels are completely separated (fully spin dependent). When $R_{\rm I} > R_{\rm I}^{\rm max}$ $R_{\rm I}$ is separated into the spin dependent/independent part.

We note that these parameters such as $\lambda_{\rm N}$, $\lambda_{\rm F}$ and $P_{\rm F}$ show exactly the same values as those from the distance dependence of NLSV signals in Ohmic F/N samples. This indicates the consistency of our results.

As shown in Fig. 3.7, both at RT and 10 K, we can reproduce the data points by the theoretical curves when $R_{\rm I}$ is below a certain value. We here define this value as $R_{\rm I}^{\rm max}$. At 10 K, $R_{\rm I}^{\rm max} = 3.0 \times 10^{-1}\Omega({\rm cm})^2$ and at RT, $R_{\rm I}^{\rm max} = 2.0 \times 10^{-1}\Omega({\rm cm})^2$. However, when $R_{\rm I} > R_{\rm I}^{\rm max}$, the experimental data level off the theoretical curves from Eq. (3.1). This indicates that it is impossible to explain the theoretical data by using Eq. (3.1) when $R_{\rm I} > R_{\rm I}^{\rm max}$, and we should reformulate Eq. (3.1) to reproduce the experimental data in $R_{\rm I} > R_{\rm I}^{\rm max}$.

In the theoretical model, as the interface resistance increases, the spin accumulation signal (ΔR) first monotonically increases and at higher $R_{\rm I}$, ΔR saturates as described by the solid curves in Fig. **??**. In this model, the change of $R_{\rm I}$ is only a nominal change of the parameter. However, in experimental situation $R_{\rm I}$ is controlled by the thickness of the insulating layer ($d_{\rm I}$). Therefore, in order to increase $R_{\rm I}$, it is necessary to increase $t_{\rm I}$. At larger $t_{\rm I}$ the spin-coherent tunneling probability decreases due to

the increasing scattering probabilities in the incularing layer. In such a high interface resistance, thus the decrease of the spin coherence needs to be considered.

This effect can be taken into account separating R_{I} into the spin dependent and the spin independent part. In the original model, R_{I} is composed only of the spin dependent part along the Valet and Felt's two currents model [74]. Thus when $R_{\mathrm{I}} < R_{\mathrm{I}}^{\max}$, R_{I} can be described as follows

$$R_{\mathrm{I}\uparrow} = \frac{R_{\mathrm{I}}}{1 + P_{\mathrm{I}0}} \tag{3.5}$$

$$R_{\mathrm{I}\downarrow} = \frac{R_{\mathrm{I}}}{1 - P_{\mathrm{I}0}}, \tag{3.6}$$

where $P_{\mathrm{I}0}$ denotes the constant spin polarization in $R_{\mathrm{I}} < R_{\mathrm{I}}^{\max}$. In this range of R_{I}, the insulating layer behaves as a complete spin filter and the spin-coherent tunneling occurs with a high probability. However, in higher R_{I}, due to the thick insulating layer, the spin-coherent tunneling is frequently interrupted and the spin filtering function declines. We define the critical value of R_{I} as $R_{\mathrm{I}}^{\max}$which separates these two different regime. Therefore when $R_{\mathrm{I}} > R_{\mathrm{I}}^{\max}$, we decompose R_{I} as the spin-dependent and the spin-independent part and describe as

$$R_{\mathrm{I}\uparrow} = \frac{R_{\mathrm{I}}^{\max}}{1 + P_{\mathrm{I}0}} + (R_{\mathrm{I}} - R_{\mathrm{I}}^{\max}) \tag{3.7}$$

$$R_{\mathrm{I}\downarrow} = \frac{R_{\mathrm{I}}^{\max}}{1 - P_{\mathrm{I}0}} + (R_{\mathrm{I}} - R_{\mathrm{I}}^{\max}). \tag{3.8}$$

From the definition of P_{I}, when $R_{\mathrm{I}} > R_{\mathrm{I}}^{\max}$ P_{I} is also affected by the redefinition of R_{I} and can be written as follows:

$$P_{\mathrm{I}} = \frac{R_{\mathrm{I}\uparrow} - R_{\mathrm{I}\downarrow}}{R_{\mathrm{I}\uparrow} + R_{\mathrm{I}\downarrow}} = \frac{P_{\mathrm{I}0} R_{\mathrm{I}}^{\max}}{R_{\mathrm{I}}^{\max} + (1 - P_{\mathrm{I}0}^2)(R_{\mathrm{I}} - R_{\mathrm{I}}^{\max})}. \tag{3.9}$$

By considering the reduction of the spin-coherent tunneling in higher R_{I} regime, we modify the theoretical curves. They are described by substituting (**??**) into (3.1) and shown with the dotted lines in Fig. **??**. It is explicitly demonstrated the reproducibility of the data in higher R_{I}. It should be noted that the data from the samples with different ds are well reproduced by the curves. We interpret the difference at 10 K and at RT in the value of $R_{\mathrm{I}}^{\max}$ as the difference in the probability of the electrons'

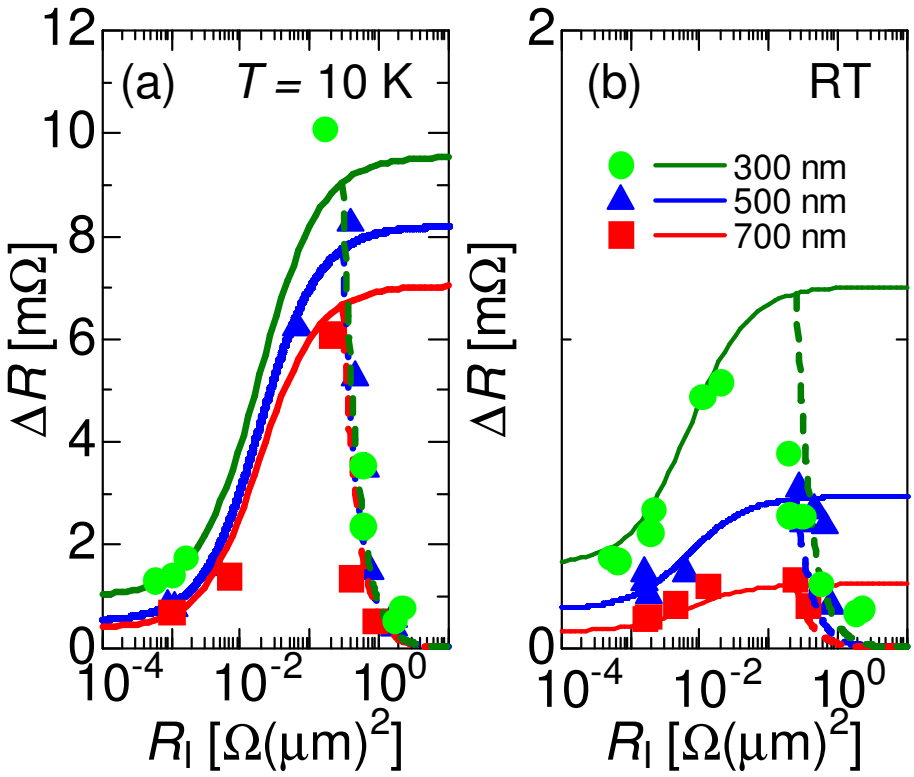

Figure 3.7: Relation between the interface resistance and the spin accumulation signal considering the modified model in $R_{\mathrm{I}} > R_{\mathrm{I}}^{\mathrm{max}}$. Dotted lines are from the new model and enable to fit data in higher R_{I} regime.

tunneling.

3.5 Summary

In this chapter we demonstrated the spin accumulation signal enhancement by means of the insertion of the insulating layer between F and N. In analogy to the TMR effect, we used the MgO layer as a tunneling layer. By modulating the thickness of the MgO layer, we were able to enhance the spin accumulation signals by a factor of ten, compared to the typical values in the NLSV samples with Ohmic F/N junction. The spin diffusion length of Cu is 1.3 μm at 10 K, twice larger than the previously obtained value in Py/Ag/Py NLSVs [45]. The dependence of the spin accumulation signal on the interface resistance can be well reproduced by using the theoretical model up to $R_{\mathrm{I}}^{\mathrm{max}}$. When $R_{\mathrm{I}} > R_{\mathrm{I}}^{\mathrm{max}}$, however, the data deviated away from the theoretical curves. This effect can be attributed to the interruption of the spin-coherent tunneling by the thicker MgO layers. By using the two current model we can consider this effect and reformulate the above theoretical model. The deviation can be explained quite well by our reformulated model.

The availability to large spin accumulation with a long spin diffusion length at a low temperature helps us progress to perform the experiments for the spin injection into the Josephson junction. We will mention this topic in the next chapter.

Chapter 4

Spin injection into Josephson junction

4.1 Motivation

Since the experimental breakthrough by Jedema *et al.*, the generation and the detection of pure spin currents have been intensively investigated in this decade. In addition to the *spin caloritronics*, which is getting a hot topic in spintronics [75, 76, 77], some applications of the spin current to induce physical phenomena must be one of the next goals in the spintronics field. Since the spin current is a flow of magnetic dipole, a phase transition relevant to the magnetism is one of the candidates for the application. In the present work, we selected the 0-π transition in the Josephson junction as a target for our research. The 0-π transition originates from the Cooper pairs with a finite momentum. This type of Cooper pair was first suggested by Fulde and Ferrell, and Larkin and Ovchinnikov independently as an inhomogeneous superconducting state (FFLO state) [78, 79]. Despite the large number of theoretical studies, it had not been experimentally demonstrated for years.

In 2001, however, Ryazanov *et al.* experimentally showed that the 0-π transition is observable through the S/F/S Josephson junction [65]. Before this discovery, an inhomogeneous superconducting state in one material rather than the multilayer structure had been studied in most cases. Owing to this work a large number of theoretical and experimental studies have been performed by using the S/F/S multilayer structure. In the S/F/S structure, there is a momentum difference between up-spin and down-spin electrons. This originates from the Zeeman split by an effective magnetic field in F. However, it is impossible to modulate E_{ex} in F continuously in such S/F/S multilayer structures. Thus there has been no research so far which clearly demonstrates the relation between the energy split (E_{ex}) by the exchange field in F and the supercurrent in the junction. In this chapter, we show the results of experiments for the ground state modulation of the Josephson junction between 0 and π by changing the spin

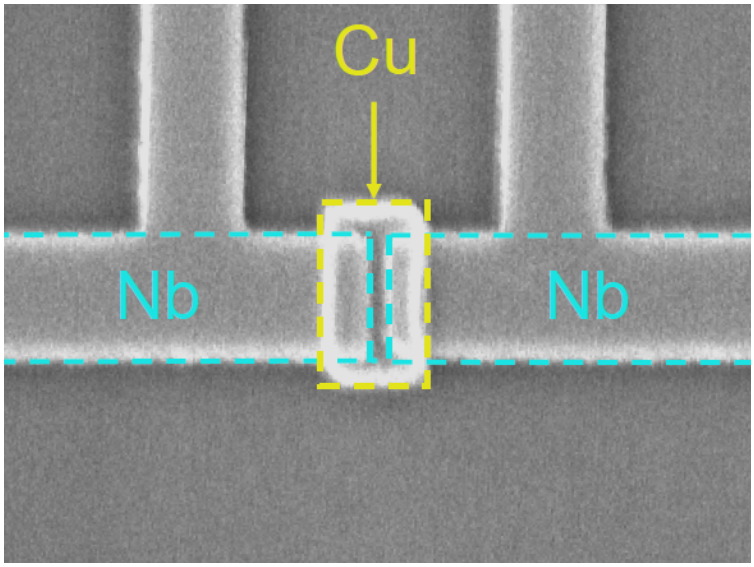

Figure 4.1: SEM image of the Josephson junction fabricated under the multi-fold liftoff process

accumulation in a lateral structure. We propose a direct way to observe the effects of the spin accumulation on the superconductivity. Details of the experiments are shown below.

4.2 Fabrication of Josephson junctions

In our experiments, we used two different techniques for fabricating the Josephson junction: a multi-fold liftoff technique and a shadow evaporation technique. We first performed a fabrication by the former technique, which is expected more easier than the shadow evaporation. In this section we show results of the Josephson junction experiments obtained from both types of the samples (i.e. fabricated by the multi-fold liftoff and the shadow evaporation process). We explain the results and compare the difference between the techniques as a result of the measured data.

In the multi-fold liftoff process, we perform a sequence of procedure (the EB lithography, the material deposition and the liftoff process) several times. Although the surface of the materials can be contaminated during the exposition to the atmosphere between subsequent sequences, depositing the materials normal to the substrate makes a flexibility to the sample structures.

We first show the fabrication process by the multi-fold liftoff process. In the Josephson junction, we use Nb as a superconductor and Cu as a normal metal. First the pattern for Nb was created by the EB lithography on the PMMA resist. Then Nb was deposited normal to the substrate. After the EB lithography for Cu, the surface of the

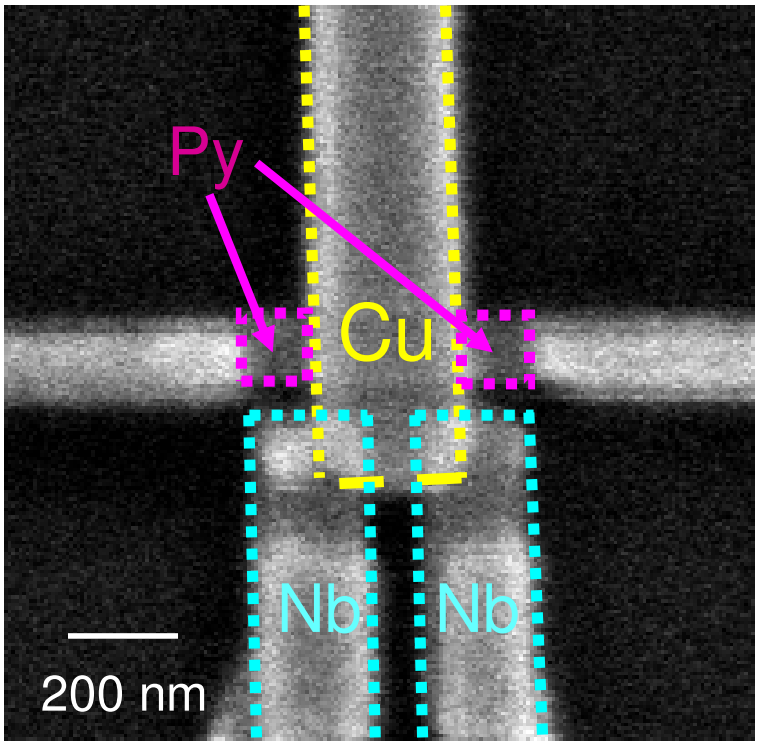

Figure 4.2: SEM image of the sample for the spin injection into Josephson junction

Nb was cleaned by the Ar ion milling. After the ion milling, the sample was transferred to another chamber and Cu was deposited normal to the substrate. We show the SEM image of the fabricated sample in Fig. 4.1. The Cu island is contacted by the two Nb banks. In the Josephson junction, the Cu island becomes superconducting by the proximity effect.

We also tried the shadow evaporation technique to fabricate the Josephson junction. Since the Andreev reflection creates Josephson junction as mentioned in the Chapter 1, a transparent contact between superconductor (S) and normal metal (N) is of importance. Therefore in order to make the interface between F and N transparent, the shadow evaporation technique is more preferable. The Josephson junction for the spin injection was therefore fabricated through the shadow evaporation technique. A SEM image of the sample is shown in Fig. 4.2. The Cu layer in the Josephson junction extends to contact the Py wire. Through the Py/Cu interface, we can inject a pure spin current into the Josephson junction. In these samples, we fabricated the Ohmic Py/Cu junction as a first step for the experiment. All fabrication processes were performed *in situ* in three steps: first Nb was evaporated to the substrate at an angle of 30° measured from the vertical axis. In order to fabricate superconducting Nb wire, we kept the evaporation rate of Nb > 2.5 Å/s. This rate was necessary for the deposition of Nb without including any impurities. After the horizontal rotation of the sample

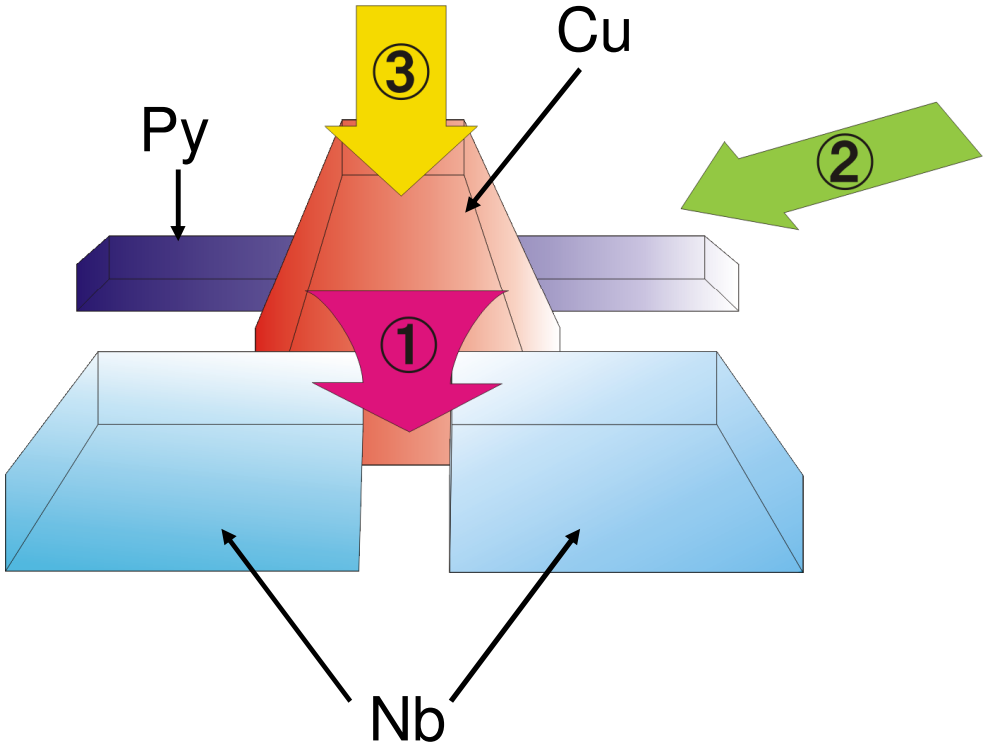

Figure 4.3: Schematic illustration of the fabrication procedure for the Josephson junction. First Nb is deposited at an angle of 30° toward the vertical axis. Then Py is deposited at 60° and then Cu is deposited normal to the substrate.

holder by 90°, then Py was evaporated at an angle of 60°. The deposition rate was in between 0.4 $\sim$ 1.0 Å/s. After transferring the sample to the other chamber, finally we deposited Cu normal to the substrate. By using this shadow evaporation technique, we can make the transparent interface between Nb and Cu. The thickness of the Py, Nb and Cu wires are 30, 20 and 100 nm, respectively. Through the interface between Py and Cu, we can inject the spin current into the Josephson junction. The schematic illustration of the procedure is shown in 4.3.

4.3 Measurements and Discussions

First we measure the Josephson junction fabricated by the multi-fold liftoff process. The measurements were performed at 350 mK, temperature low enough for the junction to become the S/N/S Josephson junction. In order to confirm that the Nb wires become superconducting, we measured the temperature dependence of the resistance of the junction. A typical curve is shown in Fig. 4.4(a). The resistance first showed a drop to almost zero. This comes from the superconducting transition of the Nb wires. Most of the T vs R curves did not show a textbook-like sharp drop at T_c (i.e. the transition temperature of the Nb wires). We attribute this to an inhomogeneity of

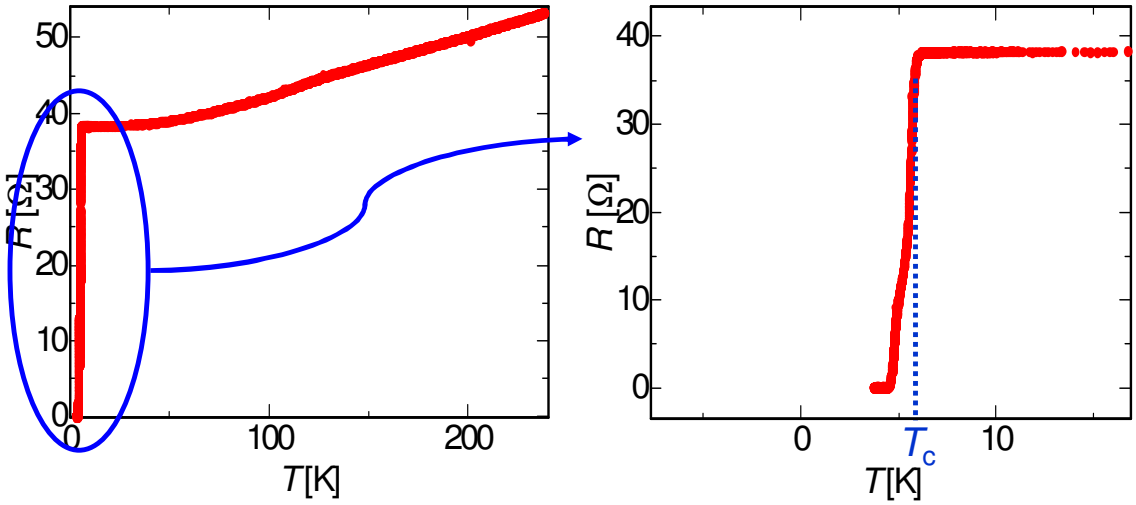

Figure 4.4: Temperature dependence of the four point resistance of the Josephson junction is shown. Although the resistance drops below 10 K, its shape is not textbook like. We define the critical temperature T_c as the point where R starts to drop.

the sample since the superconducting behavior of the Nb wire strongly depends on the evaporation condition, especially the evaporation rate. We therefore define T_c at a point where the resistance starts to drop (see Fig. 4.4(b)). Typically T_c distributes in between $5 \sim 8$ K. The remaining resistance is from the Cu wire, and it also disappeared at lower temperature due to the proximity effect.

Next we measure the IV curve of the junction at 350 mK. We flow a bias current (I) through the junction and measure the voltage between the two superconductors as shown in Fig. 4.1. A typical IV curve of the junction under I is shown in Fig. 4.5(a) and (b). When we sweep I in a wider range, the breakdown of the superconductivity of the Nb wires is explicitly seen (Fig. 4.5(a)). In this range, the IV curve shows a hysteric behavior and this means the first order phase transition of the Nb wires.

Then we focus on the I dependence of V in $I \sim 0$. In this range, we can observe the behavior of the Josephson junction: if the junction becomes the Josephson junction, supercurrent flows until the bias current reaches a critical current (I_c). Thus the voltage $V \neq 0$ derives from the breakdown of the Josephson junction (see Fig. 4.5(b)). We define I as a critical current I_c where the Josephson junction becomes an ordinary junction. As explained in the Chapter 1, I_c value is strongly related to the coupling between the two superconductors. The transparency of the interface between S and N is the most important factor for the strong coupling: in an extreme case, when the S/N junction is tunneling like, $I_c \to 0$.

We compare the properties of the junction fabricated by the multi-fold lift off process with the shadow evaporation technique. A typical difference was in the critical

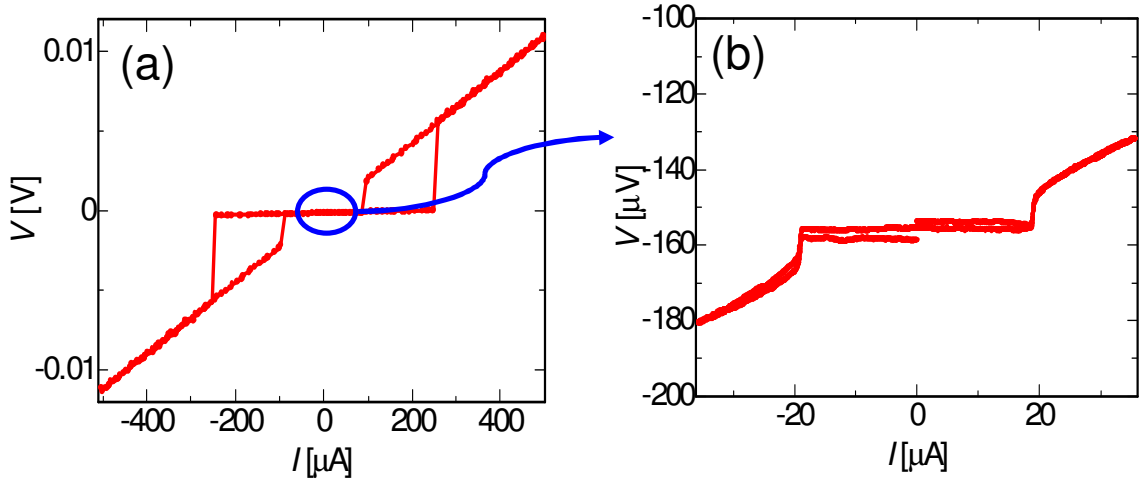

Figure 4.5: Typical IV curves of the Josephson junction. (a): In wider range of I, the curve shows a hysteric behavior. This implies the disability to dissipate heat of superconductor. (b): In narrower range of I, the critical current behavior of Josephson junction can be observed.

current of the Josephson junction as you can see in Fig. 4.6(a). The critical current of the Josephson junction fabricated by the multi-fold liftoff process showed $I_c \sim 20$ μA. On the other hand, the junction by the shadow evaporation technique had the even larger value by one order of magnitude $I_c \sim 100$ μA. You can easily confirm the difference between I_{c1} and I_{c2} in Fig. 4.6(b). Therefore we conclude that the more transparent contact is available through the shadow evaporation technique as we expected.

In the reminder of this subsection, we show the resunlts of the spin injection experiments into the S/N/S Josephson junction.

The samples were cooled down to 350 mK. The T vs R curve showed a similar behavior to our previous results. We first confirmed whether the junction becomes the Josephson junction at 350 $\sim$ 360 mK. While we flow a bias current, we measured the voltage between the two electrodes through the junction.

We demonstrate the results of the spin injection into the Josephson junction. The Josephson junctions were fabricated by the shadow evaporation technique and had a Py strip contacting to the extended Cu wire in the S/N/S junction (see Fig. 4.2). Through the Py/Cu interface, we can inject pure spin current into the Josephson junction. In order to see the effect of the spin current (the spin accumulation) on the Josephson junction, we flowed a dc current between the Cu and the Py wire, simultaneously with the bias current in the Josephson junction. If we have an effective magnetic field in the junction, this enhances the pair breaking effect. Therefore as we increase the spin injection current, the effective magnetic field in the junction also increases and the

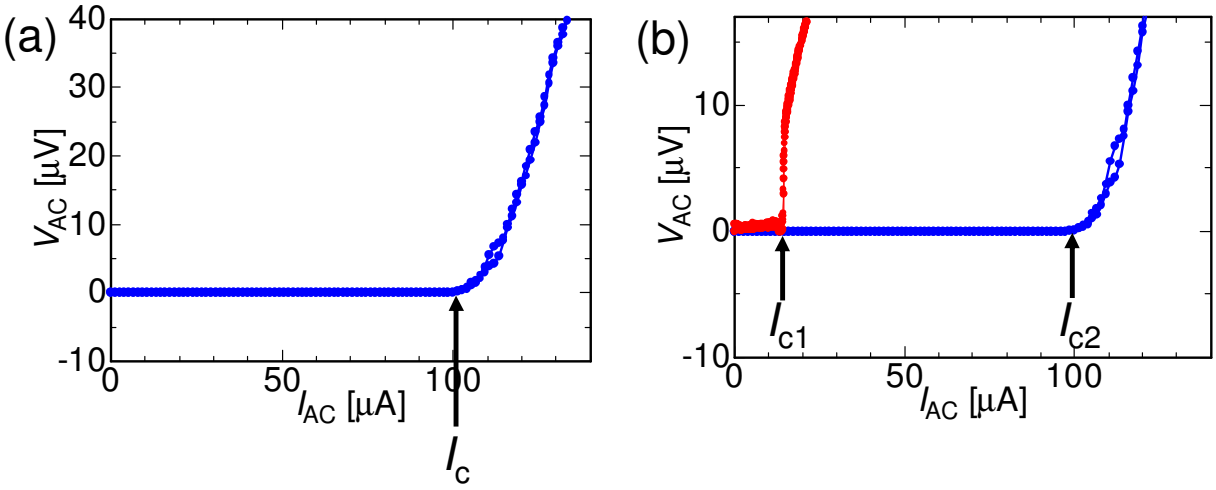

Figure 4.6: Critical current of the sample fabricated under the shadow evaporation technique. (a) Critical current is defined as the maximum bias current without generating voltage in the junction. (b) Direct comparison in the critical current betweenthe sample fabricated under the shadow evaporation technique and the multi-fold liftoff process.

coupling between the two superconductors is weaken. Since the critical current of the junction represents the strength of the coupling, the increasing spin injection current decrease the critical current.

The experimental results are shown in 4.7. As the dc current increases, we see a clear decrease of the critical current (I_c) of the Josephson junction. This represents that the coupling between the two superconductors becomes weak by the spin injection current (details are referred to the Chapter 1). We increased the dc current by a step of 1.8 μA. The relation between the spin injection current $I_{\rm dc}$ and I_c is shown in Fig. 4.7. The results were different from our expectation: the $I_{\rm dc}$ vs I_c curve did not have any cusp, which was seen in the typical 0-π transition experiments in the previous studies [65].

In order to investigate the reason for the monotonical decrease of I_c, we estimated the value of the spin accumulation necessary to induce the 0-π transition. The one-dimensional Usadel equation [80] proposes that in order to obtain the 0-π transition, the condition $\xi_1 \sim \xi_2$ should be fulfilled. Here ξ_1 and ξ_2 are the real and imaginary part of the inverse of the GL coherence length in N. Since in N, $\Psi \propto \exp(-\frac{x}{\xi}) = \exp(-\frac{x}{\xi_1})\cos(\frac{x}{\xi_2})$ the condition $\xi_1 \sim \xi 2$ means that the oscillation length (ξ_2) becomes comparable to the decay length (ξ_1). The relation between ξ and ξ_1, ξ_2 is written as

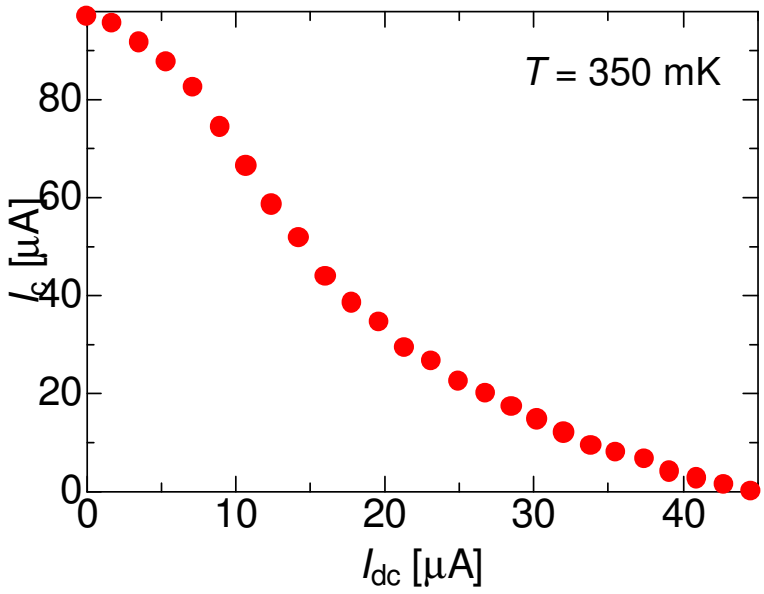

Figure 4.7: Relation between the critical current and the spin injection current. As the spin injection current increases the critical current decreases. This shows the enhancement of the pair-breaking effect with the increase of the spin injection current.

$$\frac{1}{\xi} = \frac{1}{\xi_1} + i\frac{1}{\xi_2} \tag{4.1}$$

$$\xi_{1.2} = \sqrt{\frac{\hbar D}{[E_{\rm ex}^2 + (\pi kT)^2]^{1/2} \pm (kT)^2}}. \tag{4.2}$$

Therefore at 350 mK, by substituting the experimentally obtained value into D, the condition becomes $E_{\rm ex} \gg 30$ μeV. This value is much larger than the typical spin accumulation ~ 1 μeV in our experiments.

The decrease of the critical current could attribute to the increase of the junction temperature as well as the pair-breaking effect. Thus we next investigate the heating effect by the spin injection current on the junction. Since the resistivity of Py is ten times larger than that of Cu, the Py wire could behave as a heat source when we flow a current through it.

In order to check whether the heating effect is dominant or not, we replaced the Py spin injector with the Pd wire, whose resistivity is comparable to that of Py. By changing the thickness of the Pd wire, we can make its resistance almost the same as that of the Py spin injector. In our experiments, we deposited a thinner Pd wire (60 % of the Py wire in thickness). Besides the replacement of the Py wire with the Pd one, the structure of the sample is the same. Thus we can purely investigate the heating

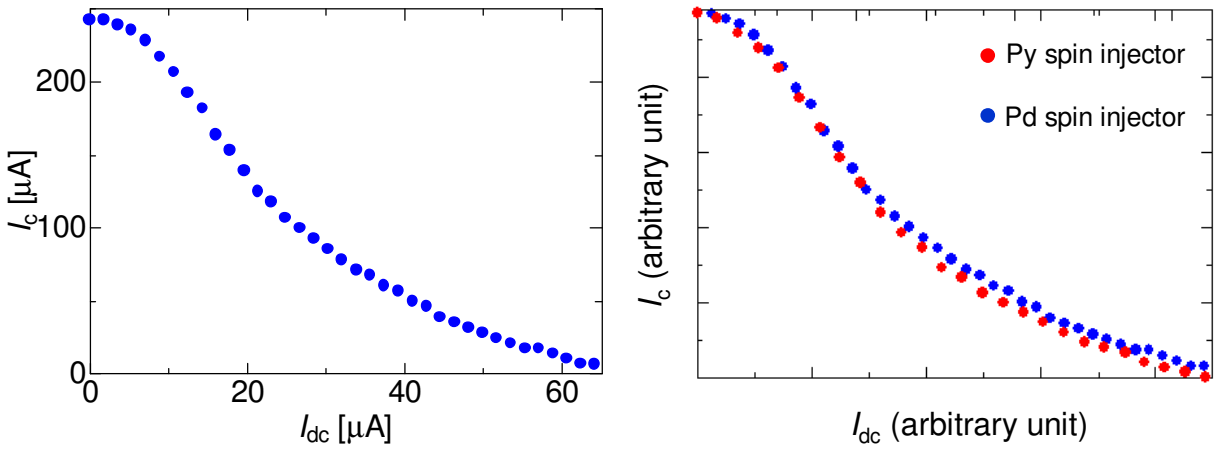

Figure 4.8: Relation between the spin injection current and the critical current. (a): I_{dc} vs I_c relation obtained from the sample with Pd spin injector. The curve shows the almost similar shape to the previous figure. (b) Comparison between the samples with Py/Pd spin injector after normalization. There is a trivial difference between them.

effect.

I_c was measured as a function of I_{dc} (defined as a current through the Pd wire in this case). The results are shown Fig. 4.8(a). As I_{dc} increases, I_c monotonically decreases. We note here that the absolute value of I_c was much larger than that obtained from the sample with the Py spin injector. Thus it is not possible to directly compare the data with the data from the sample with the Py wire.

However, we tried to compare these two data, by normalizing the data of the Pd wire to that of the sample with the Py. You can see the result in Fig. 4.8(b). The horizontal and longitudinal axis are both in an arbitrary unit. There is only a small difference between these two. As for the results from the Pd wire samples, we can rule out the effect of an effective magnetic field. Thus in the results of the samples with the Py wire, we conclude that the effect of the spin accumulation on the Josephson junction is weak.

This comparison in the experimental results between the Py wire and the Pd wire implicates that the effect of the Joule heating on the Josephson junction cannot be neglected in our experiments. Therefore it is not appropriate to apply the spin accumulation enhancement technique to the study of the spin injection into the Josephson junction. In our studies, we used the MgO layer at the N/F interface for the enhancement. However, this increases the entire resistance and thus the Joule heating. The Joule heating effect is the problem we need to solve as a future work. In the next chapter, we discuss several solutions for the suppression of the heating effect.

Chapter 5

Conclusions and Future work

5.1 Overview and Conclusion

In this section, we summarize our studies in the master degree program. The studies are composed of two parts; the enhancement of the spin accumulation and the spin injection into the Josephson junction.

Main point of the research is to induce the 0-π transition by using the spin injection technique. It is necessary to obtain the spin accumulation larger than 30 μV at 350 mK to induce the 0-π transition. Since this value is even larger than the typical spin accumulation (ΔV) for Ohmic F/N junctions, we first started to investigate the enhancement of ΔV (hereafter we use $\Delta R = \Delta V/I$ as an expression of the spin accumulation).

One of the ways to enhance ΔR is to reduce the impedance mismatch between F and N. It is theoretically predicted that the tunneling junction between F and N helps an efficient spin injection. Therefore, we inserted an insulating layer in F/N junction, and tried to enhance ΔR. In our studies, we used MgO as the insulator since it is both theoretically and experimentally demonstrated that MgO works as a good insulator for the TMR effect. The interface resistance $R_{\rm I}$ was modulated by the thickness of the MgO layer.

As we increase $R_{\rm I}$, ΔR monotonically increases when $R_{\rm I} < R_{\rm I}^{\rm max}$. When $R_{\rm I} = R_{\rm I}^{\rm max}$, ΔR reaches its maximum. The maximum values are more than ten times larger than the typical NLSV signals for the Ohmic junctions. The dependence of ΔR on $R_{\rm I}$ showed the same tendency in other samples with different separation distances (d) of two Py strips, which is quite different from the theoretical prediction. Therefore we could demonstrate the enhancement of ΔR by inserting the MgO layer between F and N.

Above $R_{\rm I} > R_{\rm I}^{\rm max}$, however, ΔR rapidly decreases as $R_{\rm I}$ increases. Thus the reformation of the theoretical model was needed. In order to explain the rapid decrease of ΔR, we assumed that the thicker MgO layer causes a spin decoherence. In this

regime, $R_{\rm I}$ can be separated into the spin-dependent part and the spin-independent part. Therefore the spin polarization of the F/N interface decreases for $R_{\rm I} > R_{\rm I}^{\rm max}$, because it is defined as $P_{\rm I} = \frac{R_{\rm I}^{\uparrow} - R_{\rm I}^{\downarrow}}{R_{\rm I}^{\uparrow} + R_{\rm I}^{\downarrow}}$. By considering the reduction of $P_{\rm I}$ in combination with the original theoretical model, we could reproduce the experimental data in three different d samples.

In order to use the spin accumulation enhancement technique for the spin injection into the Josephson junction, we next started a fabrication of the Josephson junction. Since it is difficult to fabricate the Josephson junction by using the shadow evaporation, we first tried to fabricate by the multi-fold liftoff process. Since this process usually has a disadvantage in terms of obtaining the transparent contact between S and N, the interface was cleaned by using the Ar ion milling. As a result, we measured a supercurrent under a bias current with the critical current (I_c) $\sim$ 20 μA. This demonstrates that the N part of the junction becomes superconducting, and the junction surely becomes the Josephson junction.

Next we fabricated the samples by the shadow evaporation technique. I_c reaches 100 μA, even larger than our previous results in the samples fabricated by the multi-liftoff process. This is due to more transparent S/N contacts in the shadow evaporation technique. As already mentioned in the Chapter 1, this large I_c indicates that the coupling between the two superconductors becomes even stronger (see Chapter 1). Thus we tried to inject the pure spin current into the Josephson junction fabricated by the shadow evaporation technique.

For investigating the effect of the spin injection into the Josephson junction, we measured the spin injection current $I_{\rm dc}$ dependence of I_c. With increasing $I_{\rm dc}$, I_c monotonically decreases. We can assume two different effects (pair-breaking effect) for analysing this behavior: the spin accumulation in the Josephson junction and the Joule heating due to a current in the Py spin injector. In order to see the heating effect more precisely, we replace the Py spin injector by the Pd wire. The Pd wire has almost the same resistance of the Py and we can rule out the spin accumulation effect. We obtained $I_{\rm dc}$ dependence of I_c, and compared with the previous value after the standardization. We found that these two samples show almost the same behavior. Since the Pd wire does not supply a spin current, the pair-breaking effect in the junction is mainly caused by an increasing temperature of the junction due to the Joule heating.

5.2 Future work

In the last section, we discuss our future work. As we mentioned in the Chapter 1, the next stage for spintronics is its application to other physical phenomena. In condensed matter physics, most of the novel phenomena are observed at low temperature.

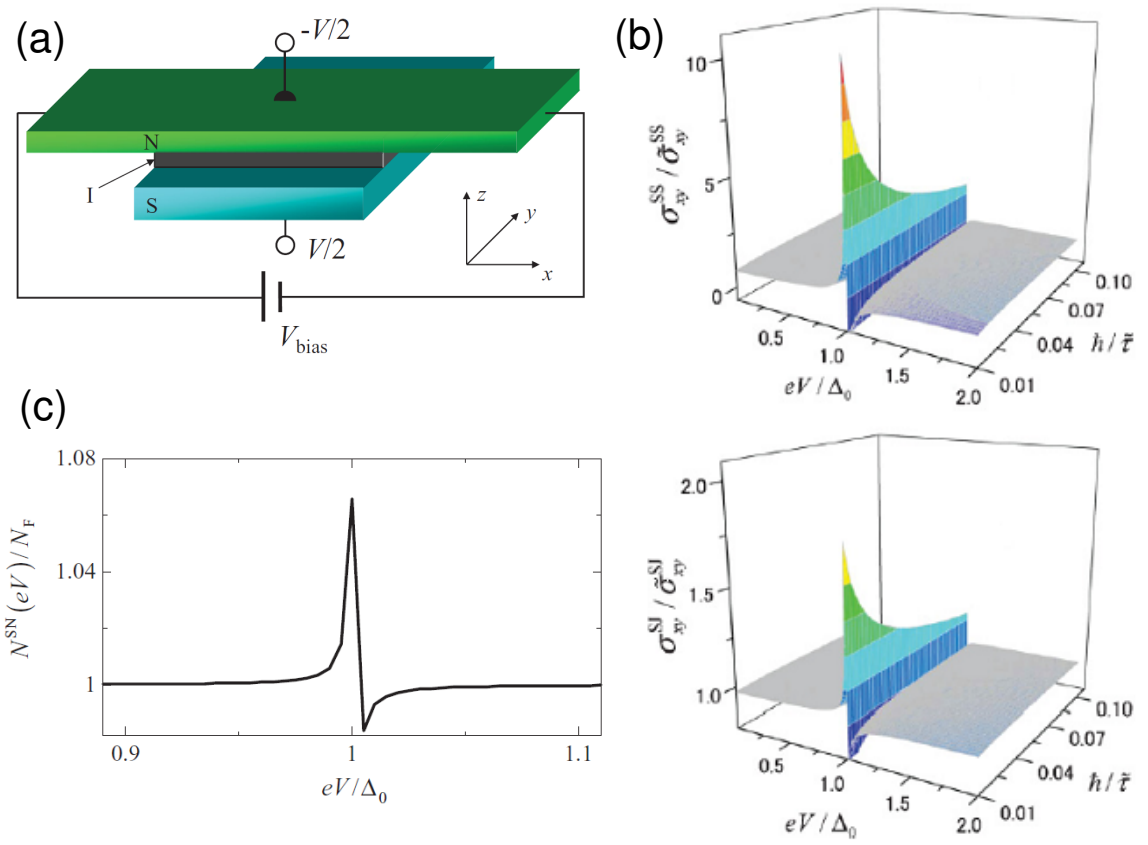

Figure 5.1: Theoretical results of the superconductivity-assisted spin Hall effect. (a): Schematic illustration of the device structure. The authors assume the direct spin Hall effect. The bias voltage is applied between S and N. Charge current simultaneously flows in N. (b): Density of states in N. As a results of resonant tunneling into S, it increases near the Fermi level. (c): Results of the calculation about the spin Hall conductivity. The spin Hall conductivity from both contributions (Skew-scattering and side-jump effect) increases reacting to the enhancement of the density of the states [82].

However, heating effects often smear such phenomena and make the detection more difficult. Thus it is essential to realize the spin injection technique at low temperature while avoiding any heating effects. As showed above, Joule heating comes from the dominant contribution of the current in F. Since we use a nonlocal measurement setup, a large current density is needed but it also increases the heating effects.

One of the solutions to reduce the Joule heating is to use a multilayer spin injector instead of a Py wire. The multilayer spin injector is a Py wire, pillowed by a nonmagnetic metal with a lower resistance such as Cu. In the injector, most current flows the Cu part and thus the Joule heating is expected to be largely suppressed.

In order to induce the 0-π transition by the spin injection, it is essential to obtain even larger ΔR. One of the ways to realize the larger value is to use a material of half-metals, in place of Py. The larger P_{F} of the half-metals is expected to enhance

ΔR in N. Such an enhancement by using the half-metals has already been reported in our collaborators. By using these two techniques, it is possible to progress our projects.

Superconductors can be used in a different way, in combination with spintronics. In spintronics the spin Hall effect is one of the promising methods for generating a pure spin current without F. The efficiency of the generation of the spin current is evaluated by the spin Hall angle ($\alpha_{\rm SH}$), the ratio of the spin Hall conductivity ($\sigma_{\rm SH}$) and the charge conductivity. Recently, the large $\alpha_{\rm SH}$ has been obtained though the extrinsic spin Hall effect in some alloys [81]. Hikino and Yunoki have suggested the anomalous spin Hall effect through the S/I/N tunnel junction [82]. Since $\sigma_{\rm SH}$ depends on the density of states (DOS) at the Fermi level of the nonmagnetic material, a larger $\sigma_{\rm SH}$ can be obtained if we can increase the DOS at the Fermi level. In the S/I/N tunnel junction, applying a bias voltage between N and S through I enhances the tunneling from S to the N. This increases the density of the states at the Fermi level in N. We note that the enhancement of the tunneling is anomalously enhanced when the Fermi level of the nonmagnetic material corresponds to the gap edge of S, where the DOS of quasiparticle in S diverges. The results of the theoretical calculations are shown in Fig. 5.1.

Spintronics with superconductivity (named as *superconducting spintronics*) contains various exciting physical phenomena and most of them are only theoretically investigated. Although the heating effect is a critical problem to be solved, an experimental realization of these phenomena is an urgent task. We believe that the experimental realization of the superconductivity spintronics opens a new way to approach the new aspects of the condensed matter physics and realize epoch-making devices such as quantum computers.

Acknowledgements

As a final chapter of my thesis I would like to express my deep gratitude to all people in our group. First of all, I am much grateful to our respectful leader, Prof. YoshiChika Otani. He gave me an opportunity to carry out the project about the latest research topic in this promising research field. His advices and suggestions are of much value and grate help for me. He took a great care of me not only for my research itself but also getting the fellowship of JSPS for my doctor degree program. Owing to his care I could experience several international conference. I would like to give a great appreciation to my direct supervisor Kohei Ohnishi. He taught me a lot from a trivial mistake in manipulating the equipments to significant thing related to research. The technique for getting a superconducting Nb was established by his great effort, which bolsters deeply my research. He is very kind and he took elaborate pains for teaching me. We know that the research of spintronics relative to the low temperature physics is quite difficult but some of his research will be inherited by me after his graduation. I am also deeply thankful to the assistant professor Yasu Niimi. His advices help me especially perform experiments well. Although he always has a lot of work he is taking care of me. I know that the modification of what I wrote is painful when I submit a paper or an abstruct to publishers, his insightful comments help me a lot. Lastly I would like to say thank you to all other people in the laboratory. Dr. Dahai wei gave me useful advices in the two years. Dr. Yasuhiro Fukuma assisted me to try to the spin accumulation enhancement experiment and had fruitful discussions. I had a great help from Dr. Shinya Kasai when I was puzzled by the results of the annealed NLSV samples. He also advices me for my future work. We had a lot of pleasant time with Dr. Tatsuya Aoki in some parties. I appreciate Mr. Satoshi Sugimoto to give me a help and have a enjoyable time especially in the first half of the two years. Mr. Hiroshi Idzuchi is a reliable person who cares me and suggests me how to generate nice data of NLSV measurements. We had a lot of suggestions from Mr. Yohei Kawanishi, Mr. Hiroshi Suzuki and Mr. Hiroaki Fujimori. Mr. Amamo Walid was a short visior but made my everyday life more enjoyable during his stay. I thank the secretary Junko Kawamura who cheered me a lot. Its a pity for me not to have data enough to analyze the effect of the spin injection on Josephson junction. The heating effect in our low

temperature experiments are to be tackled. However,its my great pleasure to have a hard but fruitful years in this laboratory and spend a great time with competent colleagues. I pay a great tribute to this laboratory and keep active in next three-year doctoral degree program.

February, 2012
on Kashiwa campus
Taro Wakamura

Bibliography

[1] I. Zutic, J. Fabian, and S. Das Sharma, Rev. Mod. Phys. **76**, 323 (2004).

[2] N. F. Mott, Proc. R. Soc. London, Ser. A **153**, 699 (1936).

[3] N. F. Mott, Proc. R. Soc. London, Ser. A **156**, 699 (1936).

[4] J. S. Moodera *et al.*, Phys. Rev. B **42**, 8235 (1988).

[5] P. M. Tedrow and R. Meservey, Phys. Rev. Lett. **29**, 192 (1971).

[6] P. M. Tedrow and R. Meservey, Phys. Rev. B **7**, 318 (1973).

[7] P. M. Tedrow and R. Meservey, Phys. Rep. **238**, 173 (1994).

[8] M. Julierére, Phys. Lett. **54A**, 225 (1975).

[9] S. Yuasa, J. Phys. Soc. Jpn. **77**, 031001 (2008).

[10] M. N. Baibach *et al.*, Phys. Rev. Lett. **61**, 2472 (1988).

[11] W. P. Pratt *et al.*, Phys. Rev. Lett. **66**, 3060 (1991).

[12] M. A. M. Gijs and G. E. W. Bauer, Adv. Phys. *46*, 285 (1997).

[13] J. Mathon and A. Umerski, Phys. Rev. B, *56*, 11810 (1997).

[14] S. S. P. Parkin, R. Bhadra and K. P. Roche, Phys. Rev. Lett. **66**, 2152 (1991).

[15] S. S. P. Parkin, Z. G. Li and D. J. Smith, Appl. Phys. Lett. **58**, 2710 (1991).

[16] W. H. Butler *et al.*, Phys. Rev. B **63**, 054416 (2003).

[17] S. Yuasa *et al.*, Nat. Mater. **3**, 868 (2004).

[18] S. S. P. Parkin *et al.*, Nat. Mater. **3**, 862 (2004).

[19] M. Johnson and R. H. Silsbee, Phys. Rev. Lett. **55**, 1790 (1985).

[20] N. Hass *et al.*, Physica C **235**, 1905 (1994).

[21] Z. W. Dong *et al.*, Appl. Phys. Lett. **71**, 1718 (1997).

[22] V. A. Vas'ko *et al.*, Phys. Rev. Lett. **78**, 1134 (1997).

[23] N. -C. Yeh *et al.*, Phys. Rev. B **60**, 10522 (1999).

[24] P. R. Hammer *et al.*, Phys. Rev. Lett. **83** 203 (1999).

[25] F. G. Monzon and M. L. Roukes J. Magn. Magn. Mater. **199** 632 (1999).

[26] H. J. Zhu *et al.*, Phys. Rev. Lett. **87** 016601 (2001).

[27] M. Johnson, Science **260**, 320 (1993).

[28] J. M. Kikkawa and D. D. Awschalom, Nature **397**, 139 (1999).

[29] R. Fiederling *et al.*, Nature **402**, 787 (2000).

[30] I. Malajovich, J. M. Kikkawa and D. D. Awschalom, Phys. Rev. Lett. **84**, 1015 (2000).

[31] J. Fabian and S. Das Sharma, J. Vac. Sci. Technol. B **17** 1708 (1999).

[32] R. J. Elliott, Phys. Rev. **96**, 266 (1954).

[33] Y. Yafet, *Solid State Physics, Vol. 14*, edited by F. Seitz and D. Turnball (Academic, New York, 1963).

[34] F. Beuneu and P. Monod, Phys. Rev. B **18**, 2422 (1978).

[35] M. I. D'yakonov and V. I. Perel', Sov. Phys. Solid State **13**, 3023 (1971).

[36] G. L. Bir, A. G. Aronov and G. E. Pikus, Zh. Eksp. Teor. Fiz. **69**, 1382 (1975).

[37] M. I. D'yakonov and V. I. Perel', Sov. Phys. JETP **38**, 362 (1973).

[38] A. W. Overhauser, Phys. Rev. **89**, 689 (1953).

[39] F. J. Jedema, A. T. Filip and B. J. van Wees, Nature **410**, 345 (2001).

[40] F. J. Jedema *et al.*, Nature **416**, 713 (2002).

[41] S. Takahashi and S. Maekawa, Phys. Rev. B **67**, 052409 (2003).

[42] S. Takahashi and S. Maekawa, Sci. and Tech. of Adv. Mater. **9**, 014105 (2008).

[43] G. Schmidt *et al.*, Phys. Rev. B **62**, 4790 (R) (2000).

[44] E. I. Rashba, Phys. Rev. B **62**, 16267 (R) (2000).

[45] Y. Fukuma *et al.*, Appl. Phys. Lett. **97**, 012507 (2010).

[46] Y. Fukuma *et al.*, Nat. Mater. **10**, 527 (2011).

[47] H. Kamerlingh Onnes, *Laiden Comm.* **120b**, **122b**, **124c** (1911).

[48] M. Tinkham, *Introduction to Superconductivity, 2nd Ed.* (Dover, New York, 2004).

[49] J. G. Bednorz and K. A. Müller, Z. Phys. B **64**, 189 (1986).

[50] V. L. Ginzburg and L. D. Landau, Zh. Eksperim. i. Teor. Fiz. **20**, 1064 (1950).

[51] J. Bardeen, L. N. Cooper and J. R. Schrieffer, Phys. Rev. **108**, 1175 (1957).

[52] L. N. Cooper, Phys. Rev. **104**, 1189 (1956).

[53] B. D. Josephson, Phys. Lett. **1**, 251 (1961).

[54] B. D. Josephson, Adv. Phys. **14**, 419 (1965).

[55] W. C. Stewart, Appl. Phys. Lett. **12**, 277 (1968).

[56] D .E. McCumber, J. Appl. Phys. **39**, 3113 (1968).

[57] A. F. Andreev, Zh. Eksp. Teor. Fiz. **46**, 1823 (1964).

[58] G. E. Blonder, M. Tinkham and T. N. Klapwijk, Phys. Rev. B **25**, 4515 (1982).

[59] H. Sellier *et al.*, Phys. Rev. B **68**, 054531 (2003).

[60] L. N. Bulaevskii, V. V. Kuzii, and A. A. Sobyanin, JETP Lett. **25**, 290 (1977).

[61] A. I. Buzdin, L. N. Bulaevskii, and S. V. Panjukov, JETP Lett. **35**, 178 (1982).

[62] A. I. Buzdin, B. Bujicic, and B. M. Yu. Kupriyanov, Sov. Phys. JETP **74**, 124 (1992).

[63] E. A. Demler, G. B. Arnold, and M. R. Beasley, Phys. Rev. B **55**, 15174 (1997).

[64] M. Eschrig, Physics today **64**, 43 (2011).

[65] V. V. Ryazanov *et al.*, Phys. Rev. Lett. **86**, 2427 (2001).

[66] V. A. Oboznov *et al.*, Phys. Rev. Lett. **96**, 197003 (2006).

[67] T. Kontos *et al.*, Phys. Rev. Lett. **89**, 137007 (2002).

[68] Y. Blum *et al.*, Phys. Rev. Lett. **89**, 187004 (2002).

[69] J. W. A. Robinson *et al.*, Phys. Rev. Lett. **97**, 177003 (2006).

[70] A. I. Buzdin, Rev. Mod. Phys. **77**, 935 (2005).

[71] F. S. Bergeret, Rev. Mod. Phys. **77**, 1321 (2005).

[72] T. Yamashita, S. Takahashi and S. Maekawa, Phys. Rev. B **73**, 144517 (2006).

[73] T. Yamashita *et al.*, Phys. Rev. Lett. **95**, 097001 (2005).

[74] T. Valet and A. Fert, Phys. Rev. B **48**, 7099 (1993).

[75] K. Uchida *et al.*, Nature **455**, 778 (2008).

[76] K. Uchida *et al.*, Nat. Mater. **9**, 894 (2010).

[77] *Spin Caloritronics*, *Special Issue of Solid State Communications*, edited by G. E. W. Bauer, A. H. MacDonald and S. Maekawa (Elsevier, 2010).

[78] P. Fulde, R. A. Ferrell, Phys. Rev. **135**, A550 (1964).

[79] A. I. Larkin and Y. N. Ovchinnikov, Sov. Phys. JETP **20**, 765 (1965).

[80] K. D. Usadel, Phys. Rev. Lett. **25**, 507 (1970).

[81] Y. Niimi *et al.*, Phys. Rev. Lett. **106**, 126601 (2011).

[82] S. Hikino and S. Yunoki, Phys. Rev. B **84**, 020512 (2011).